

TESTBED DESIGN FOR INVESTIGATING THE IRRADIANCE AND INTENSITY UNIFORMITY  
PERFORMANCE OF LIGHTPIPES

by

Jared Talbot

---

Copyright © Jared Talbot 2019

A Thesis Submitted to the Faculty of the

COLLEGE OF OPTICAL SCIENCES

In Partial Fulfillment of the Requirements

For the Degree of

MASTER OF SCIENCE

In the Graduate College

THE UNIVERSITY OF ARIZONA

2019

THE UNIVERSITY OF ARIZONA  
GRADUATE COLLEGE

As members of the Master's Committee, we certify that we have read the thesis prepared by **Jared Talbot** titled ***Testbed Design for Investigating the Irradiance and Intensity Uniformity Performance of Lightpipes*** and recommend that it be accepted as fulfilling the thesis requirement for the Master's Degree.

  
\_\_\_\_\_  
**Dr. John Koshel**

Date: **5/1/2019**

  
\_\_\_\_\_  
**Dr. Mary Turner**


Date: **5/1/2019**

  
\_\_\_\_\_  
**Dr. Jose Sasian**

Date: **5/1/2019**

Final approval and acceptance of this thesis is contingent upon the candidate's submission of the final copies of the thesis to the Graduate College. ®

I hereby certify that I have read this thesis prepared under my direction and recommend that it be accepted as fulfilling the Master's requirement.

  
\_\_\_\_\_  
**Dr. John Koshel**  
**Associate Dean of Academic Programs**  
**Professor**  
**Optical Sciences**

Date: **5/1/2019**

# Acknowledgements

Firstly, I would like to express my deepest gratitude to my advising Professor Dr. John Koshel for his continuous support, insight, and guidance throughout the course of my thesis work. Completing a thesis at a distance student has the potential to complicate simple logistical things quite a bit, but Dr. Koshel was always available and flexible. He consistently asked questions which pushed me to thinking deeper and while still allowing me the freedom to make this work my own. I could not have imagined a better advisor.

I would also like to thank the rest of my committee members, Dr. Mary Turner and Dr. Jose Sasian. Dr. Turner is not only a committee member, but a trusted colleague. She too was continually available to answer questions and provide guidance throughout my thesis and overall graduate work. Dr. Sasian graciously agreed to join my committee and is one of my favorite professors from my coursework. The enthusiasm with which he teaches is second to none and something I truly appreciated as a student.

Last I would like to thank Edmund Optics Inc. and my colleagues there. The company has supported me throughout my graduate work, specifically Joel Bagwell, Jeremy Govier, Scott Sparrold, Nathan Carlie, Pat McKenna, and Andrew Lynch.

# **Dedication**

This thesis is dedicated to my loving wife Dominique. I would not be where I am today without her by my side during this journey to support and encourage me.

# Table of Contents

1) List of Figures .....	7
2) List of Tables .....	9
3) Abstract .....	10
4) Introduction .....	11
5) Theory .....	26
a. Lightpipes, Uniformity, & Illumination Mixing Concepts .....	26
b. Integrating Spheres .....	32
c. Bidirectional Reflectance Distribution Function (BRDF) .....	33
d. System Architecture Options .....	35
6) Materials and Methods .....	42
a. Radiometer Based Point-by-Point Scanning Collection Systems .....	42
b. Detector Array & Imaging Based Collection Systems .....	46
c. Incoherent Illumination System for Uncertainty Determination .....	47
d. Coherent Illumination System for Testing .....	47
e. Image and Data Analysis .....	49
7) System Comparison & Selection .....	53
a. Review of System Tradeoffs .....	53
b. Angular Uniformity Noise Determination & Comparison .....	54
c. Spatial Uniformity Noise Determination .....	58
8) Experimentation .....	59

a. Background .....	59
b. Results .....	60
9) Conclusions & Future Considerations .....	69
10)References .....	75
11)Appendix A: Hypercentric Lens Data .....	78
12)Appendix B: Radiometer RSS Line-Of-Sight (LOS) Error .....	79

# List of Figures

1) Example of LED DLP Projector Layout .....	12
2) Example of Laser DLP Projector Layout .....	13
3) Planarian Neoblasts .....	17
4) Basic Layout of a Flow Cytometer .....	18
5) Flow Cell Illumination Examples .....	20
6) Example of Beam Combining & Separating .....	23
7) Flow Cytometer Layout Using a Lightpipe .....	24
8) Lightpipe Illuminance Superposition .....	28
9) Square vs Square-Microstructured Lightpipe .....	29
10) Effects of a Decenter Lightpipe .....	30
11) Collimated vs Converging Cellular Excitation Beam .....	34
12) Hypercentric Lens Diagram & Example Image .....	40
13) Scanning & Imaging System Layouts .....	45
14) Coherent Illumination Layout .....	48
15) “Unwrapping” the Polar Image .....	50
16) Pixelated Example of “Unwrapping” .....	51
17) Layouts for Determining Noise Levels .....	54
18) Angular Data Comparison .....	56
19) Analysis of Hypercentric Imaging System’s Integrating Sphere Data .....	57
20) Lightpipe Case Study Candidates .....	59

21) “Unwrapping” Process of the Tapered Lightpipe Output .....	60
22)Change in Uniformity vs Numerical Aperture .....	61
23)Change in Uniformity vs Input Angle .....	62
24)Summary of CV Data for Angular Uniformity Measurements .....	64
25)Summary of CV Data for Spatial Uniformity Measurements .....	65
26)Summary of PSD Data for Spatial Uniformity Measurements .....	67
27)Non-Sequential Modeling of Alignment Errors .....	72



# List of Tables

1) PCX Lens Radiometer Tolerance Table .....	26
2) Radiometer Yield Results .....	27

# Abstract

The following describes the design for a low cost optical testbed tailored to measure the irradiance and radiant intensity uniformity of the light field output from a lightpipe. The testbed has been designed to be flexible from a mechanical standpoint to accommodate straight and tapered lightpipes with a varying number of sides and lengths, so that it can serve as a general test setup for various lightpipes which need to be validated and inspected for their output irradiance and radiant intensity uniformity performance. Key application spaces where uniformity of the irradiance and radiant intensity of the lightpipes output are critical, are flow cytometry and digital light projectors, are discussed. The ideal resolution required of the testbed is derived based on the functional requirements for the key applications. It is necessary to determine the level of accuracy needed in the testbed to ensure performance of the flow cytometer or digital light projector are not limited by the performance of the lightpipe.

Two system architecture options are proposed, with low cost versions of each built and tested. Experimental data is collected with both systems and a common standard is used to compare the two and select the best option for a low cost system. The selected system is then put through additional experimental testing to explore its utility in comparing the measured performance of two well understood lightpipe designs, which are the square tapered lightpipe and the hexagonal lightpipe. All of these results are then discussed, and future improvements considered.

# Introduction

Over the past few years there have been significant improvements in illumination sources, as well as the development and growth of applications spaces in which they are used. From improvements that have allowed for the size and cost of laser diode models to be driven down, to an increase in the efficiency of light-emitting diodes (LEDs), as well as many other innovations make it more cost feasible for the optical designer to integrate these types of light sources into smaller cost sensitive systems, where it previously was impractical to use them. In many of these cases it is now feasible, from a cost and space perspective, to integrate multiple narrow spectrum emitters in a single system to meet the full spectrum needs of the system, as an alternative to using traditional broadband incandescent sources in conjunction with a set of filters. Because of this, in general, LEDs have replaced incandescent lamps for most applications and are now the most common light sources used with lightpipes [1].

For applications where the lightpipe is only required to transport light without any specific uniformity requirements this integration of multiple emitters is fairly easy. However, in applications where the systems functionality is dependent upon how these separate sources are combined together from an irradiance and radiant intensity perspective it is crucial for the lightpipe design to control this mixing. Therefore, in order for these types of sources to be used in these applications, the need for components that can precisely combine input sources is critical, as are testing solutions to verify these components are manufactured correctly. Among the various application spaces that

present this need, this testbed has been designed to validate combining solutions for two specific applications. The areas which this testbed addresses are lightpipes for digital cinema (LCD and DMD Projectors) and life sciences (flow cytometers and fluorescence microscopes).

In digital cinema there is a lot of development being done to use integrated lasers systems (i.e., coherent radiation) instead of normal lamp based or LED based systems such as the one shown in Figure 1 (i.e., incoherent radiation). Using separate red, blue, and green input sources offers a significant improvement over a normal broadband lamp in the power efficiency of the system, making LED or laser diodes based solutions ideal [2]. Taken a step further in a comparison of laser diodes based systems versus LED based systems, it has been shown that laser diode projectors offer a longer lifetime and better color quality [2] [3] [4].

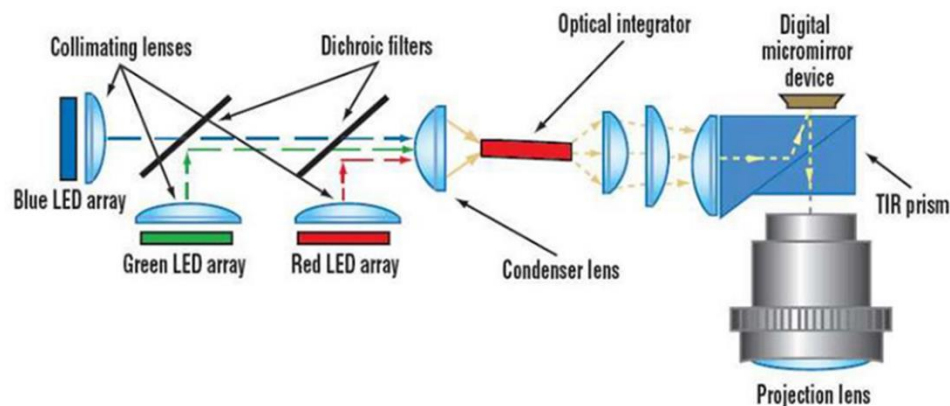


**Figure 1 – Example LED DLP Project Layout:** Shows one possible version of an LED based DLP projector. In this example each LED has its own collimating lenses and dichroic filters, which are used to combine the collimated beams. The lightpipe is used for the mixing of the combined beams. The mixed output of the lightpipe is then

sent to the digital micromirror device (DMD) in the system and then outputted to the projection lens [5].

Here, the color tuning range offered is critical to the performance of these types of projectors, and with laser diodes offering narrower well-defined bandwidths compared to LEDs the control of the colors generated is greater. Hence, the uniformity and range of the color tuning offered by combining optical elements must match that of the light modulator and the level that a human observer sees with their eye. Typically a system of dichroic filters or a fiber combiner is needed to combine the input laser beams of the system, while still requiring a lightpipe and additional optics to mix, homogenize the combine beam. From a cost perspective it would be advantageous if there were an alternative solution that was able to homogenize, combine, and despeckle them with only a lightpipe and focusing element. In either case there is a clear need for a testing method to ensure that the optical train design has successfully created uniform irradiance and radiant intensity profiles upon the lightpipe.

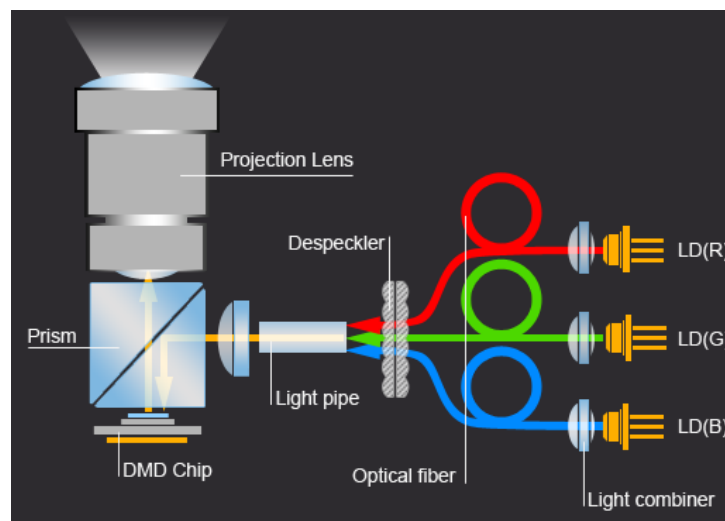


**Figure 2 – Example Laser DLP Projector Layout:** Shows a laser based RGB DLP projector. In this example the lasers are fiber coupled and brought together via a fiber combiner. The output of the fiber is then passed through a despeckling element and lightpipe prior to being directed toward the DMD chip [4].

In these systems the projection lens is going to offer higher resolution than the DMD it is paired with making the spatial resolution limited by the resolution of the DMD. To understand the range of resolutions offered by DMDs, we will take a look at the offering from one of the main manufacturers, Texas Instruments. Specifically the DLP660TE from Texas Instruments, a DLP designed for 4K UHD digital projectors will be considered. This is a market leading DLP in terms of resolution. This device contains  $5.4\ \mu\text{m}$  micromirrors which offer a  $\pm 17$ -degree tilt range [6]. This would mean that in order to have a spatial resolution measurement with a level of fidelity which is ten times that of the DMD we need to be able to measure the spatially uniformity down to  $0.54\ \mu\text{m}$ .

This can be taken a step further by examining the lateral color requirements of the projection lenses typically used in these system. Most projection lenses are required to provide  $< 1/2$  of a pixel of lateral color from 460nm to 620nm and  $< 2/3$  of a pixel of lateral color from 430nm to 670nm, in order to ensure that pixel color artifacts are not produced [7]. That means that in order to ensure the uniformity of lightpipe output is high enough to avoid causing the same type of artifact, it is necessary to, measure spatial uniformity down to  $0.27\ \mu\text{m}$ .

In regards to the angular uniformity requirements for DLP projectors, the Texas Instruments DMD again provides guidance. As mentioned previously that device offers +/- 17 degrees of movement for the micromirrors inside. This can be considered to be representative of the type of angular range over which the light source in these devices will need to be uniform, providing a minimum angular measurement range the testbed must cover. A quick review of projection lenses available for 4K UHD projectors confirms this as they are offered with f-numbers in the range of  $f/1.7$ - $1.8$  [8, 9]. A first-order calculation to convert the +/- 17 degrees of the DLP to the possible cone angle output by the DLP we get an  $NA$  of 0.2924, where

$$NA = n * \sin \theta \quad (1)$$

Then if we assume that the focal length of the projection lens is under 50 mm and that minimum working distance is around 5 meters, at least two orders of magnitude larger, we can use the following relationship:

$$NA \approx \frac{1}{2*f/\#} \quad (2)$$

to approximate the f-number with a high degree of accuracy, assuming operation at infinite conjugates, as this is in the hyperfocal regime. Using an  $NA$  of 0.2924 this calculation yields an estimated required f-number of 1.71, which agrees with the projector lenses available and confirms the need to sample over a +/- 17 degrees angular range. In terms of the level of uniformity needed, studies have shown that slow variations across the diagonal of the screen have an allowable non-uniformity of 33% while the typical brightness uniformity being marketed by the projection companies is 90% [8].

In life sciences there is a similar need for combining multiple illumination sources, which can be LED or laser based, that are used as excitation sources in flow cytometers. Flow cytometry is a technique widely used in the medical and life sciences communities to provide, at high throughput rates, simultaneous information about multiple cell characteristics. Researchers in fields such as stem cell research, tissue regeneration, cellular morphogenesis, genetics, and pharmaceuticals, as well as clinicians monitoring CD4 cell counts in HIV patients, performing skin biopsies, and identifying subtypes of inflammatory cells in lupus patients regularly use this technique in their daily work [10]. A flow cytometer provides measurements on cells surface morphology, protein composition, nucleus composition, and cell cycle, among many other things. By measuring these characteristics on individual cells it provides the ability to characterize entire populations of heterogeneous cells to provide a breakdown on the makeup of the population [10].

For example, flow cytometers are frequently used in the genetics research surrounding the stem cell population of planarians. Planarians are flatworms which have two very distinct features. First, they can regenerate due to a high stem cell population, which are called neoblasts. Second, there are strands which have their entire genome sequenced making them ideal for research regarding tissue regeneration and cellular differentiation. For researchers interested in trying to understand how the regeneration process works, isolating the neoblast population from the other cells for a particular experiment may be necessary. Neoblasts can be uniquely identified and sorted using a flow cytometer based on their 6-10um size and high nucleus (round organelle containing the genetic material of a cell) to cytoplasm (material within a cell outside of the nucleus) ratio



(Figure 3) [11]. To better understand how the flow cytometer is able to measure these two parameter we will need to take a closer look at how the flow cytometer works.

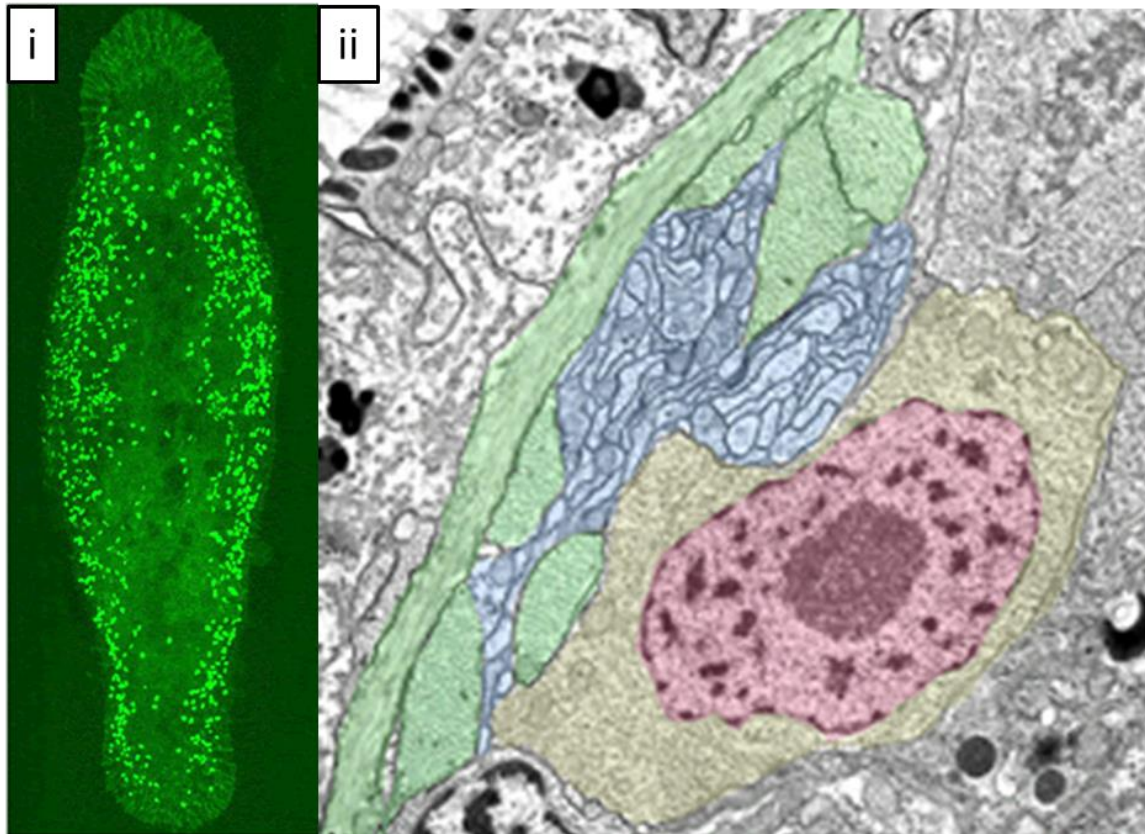


**Figure 3 – Planarian Neoblasts:** (i) show an image of a planarian which has had its neoblasts labelled with a green fluorescent marker, with figure 3(ii) showing an image of an individual neoblast where the nucleus is shown in red and the cytoplasm shown in yellow [11].

The process starts with a population of dissociated cells suspended in a solution which is loaded into the flow cytometer. This cell suspension solution is passed through a microfluidics system containing a nozzle which creates hydrodynamic focusing to produce

a single file stream of cells [12]. These individual cells are then passed through a converging beam of light as shown in Figure 4, which in this case is made up of 2 laser beams which have been combined using a dichroic filter. As the cells pass through the converging beam of light a few things will happen. Some of the light will transmit through the cell and undergo what is called volume scattering where the composition of the cell causes the transmitting light to diffuse. This light is captured by the forward-scatter detector (FSD) in the system and will help to determine the size of the cell.

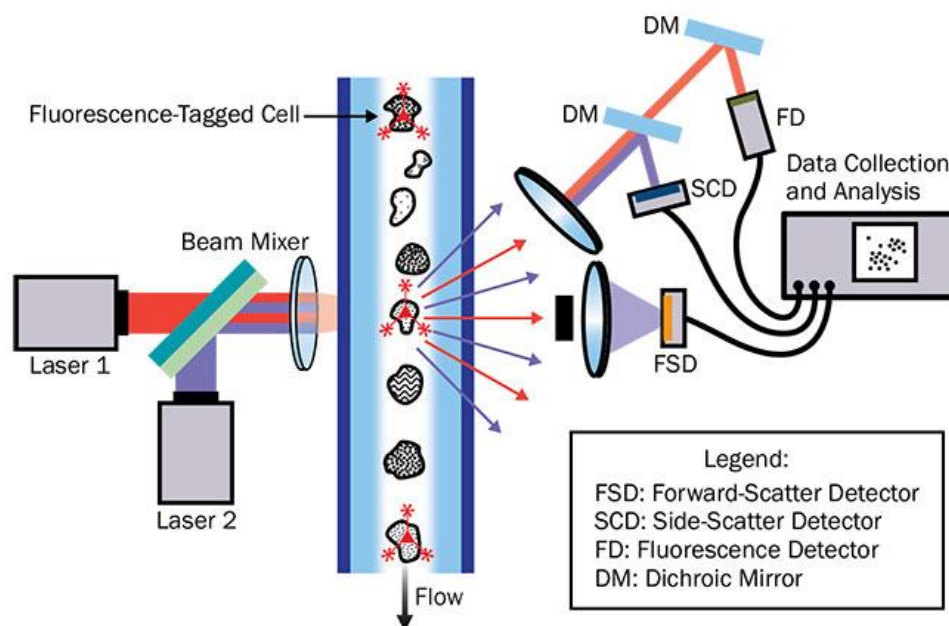


**Figure 4 – Basic Layout of a Flow Cytometer:** Schematic showing a generic flow cytometer system. Here two excitation lasers are combined using a dichroic filter. The combined beam is then focused by a lens making it a converging beam which is passing through the flow cell. As cells pass through the flow cell they are illuminated by this converging beam. Some of the light is transmissively scattered into the forward

scatter detector (FSD), which is in the same direction as the excitation path. Another portion of the light is reflected sideways off the cell surface into the side scatter detector (SCD). Last, a portion of the light is also absorbed by the fluorescent material the cells have been tagged with which can be a dye, antibody stain, etc. This fluorescent material will then have an emission which is collected by the fluorescent detector (FD) [13].

A portion of the converging beam will also diffusely reflect off of the cell surface toward the side-scatter detector (SCD) in the system. The light collected by the SCD also helps to determine the size of the cell as well as the composition of the surface. Last, if antibodies or dyes have been applied to the cell a portion of the light will be absorbed by these markers and a fluorescent emission will be produced which is also collected by the side-scatter channel but directed to a fluorescent detector (FD) via a dichroic filter. In the case of sorting for the neoblast population as discussed earlier, there would be two fluorescence detectors, one for measuring the fluorescent emission for a marker specific to the nucleus and another for measuring the fluorescent emission specific to the marker for the cytoplasm. The ratio of the strength of these two signals is representative of the size of each region, allowing for the cytoplasm to nucleus ratio to be calculated.

Since the strength of the fluorescent emission is directly tied to the excitation, any bias in excitation light the sample sees from one of the input sources over another degrades the resolution of the system. Therefore, uniformity of the illumination from each source is critical. Spatially the beam needs to be uniform across the width of the flow cell, as well as along the direction of the cell flow. However, in an ideal state the beam will be narrow

enough along the direction of the cell flow so that only one cell is interrogated at a time.

Figure 5 illustrates this with 3 example incident beams. The first is a small circular beam which is 20 $\mu$ m in diameter, which is able to illuminate one cell at a time but does not do so in a spatially uniform fashion. The second beam is larger circular beam 60 $\mu$ m in diameter, which now provides a more spatially uniform source of illumination across the flow cell but is large enough that multiple cell are illuminated at the same time. The third beam is elliptical in shape (60 $\mu$ m wide x 20 $\mu$ m tall) enabling it to uniformly illuminate across the flow cell while still being narrow enough along the direction of the flow cell to only illuminate one cell at a time.

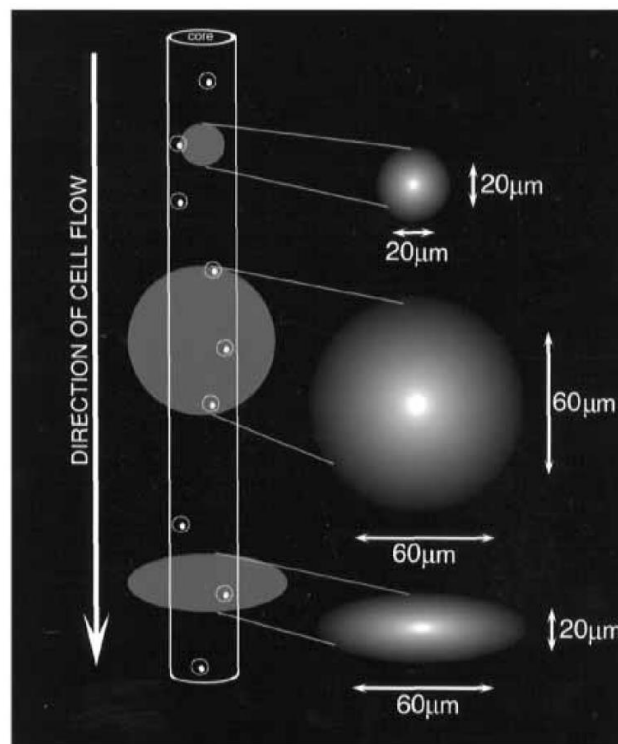


**Figure 5 – Flow Cell Illumination Examples:** Illustrates 3 example illumination beams. One which is circular and too small to uniformly illuminate the flow cell, one which is circular and too large to illuminate a single cell at time, and one which is

elliptical and able to both uniformly illuminate the flow cell while also only illuminating one cell at a time [14].

Having detailed why spatial uniformity is critical to the performance of flow cytometry it is not necessary to define the level of spatial uniformity necessary by examining a commercially available unit like the S1000EXi from Stratadigm. This system offers the ability to detect particles as small as 0.5  $\mu\text{m}$  on the FSD and 0.2  $\mu\text{m}$  on the SCD, which is verified by calibrating the system via fluorescently labelled polystyrene beads of those sizes [15]. The use of polystyrene beads in this fashion is standard practice within flow cytometry, where these tightly toleranced beads serve as resolution and instrument sensitivity calibration standards the same way a standard vision system might be calibrated using USAF targets and reflectance standards. Ideally the resolution of the spatial uniformity measurement will be at least 0.2  $\mu\text{m}$ .

Also, in an ideal situation this calibration will be done with beads which all have the exact same size and intrinsic fluorescent response, however, in practice this is not the case. Depending on the size of beads being used for this calibration their intrinsic fluorescent response can vary between 3% to 14%, which correlates to the reported variation of beam intensity across the flow cell of 13% [16] [17] [18]. If we take this 14% variation to be representative of the accuracy of the uniformity calibration of the flow cytometer, then this is also the level of spatial uniformity down to which we must be able to measure. While this clearly shows how spatial uniformity is of the utmost importance, angular uniformity is also very important when considering the SCD. Being that the input beam in the system is typically a converging, this means that there will be an angular range associated with it.

Without the converging beam being angularly uniform it will have an effect on the anticipated bidirectional reflectance distribution function (BRDF), which we will discuss in more detail in the theory section later on.

Now that we reviewed the flow cytometer in full and its illumination requirements I would like to ask the question, are there areas in which we can potentially make the system more cost efficient? To answer this questions let us focus on the illumination portion of the system the dichroic filters shown in figure 4 which are used in most systems for beam combining. While the basic system we reviewed in Figure 4 only has two excitation sources, requiring a single dichroic filter for combing the excitation beam and one for separating the light directed toward the SCD and FDAs, many systems on the market actually have additional laser sources. In fact, the S1000EXi from Stratedigm we discussed earlier is one which supports up to four lasers, with standard options at 405 nm, 488nm, 532 nm, and 640 nm while custom options are also available at 372 nm, 552 nm, 561 nm, and more available upon request [9].

The reason for is that while there are many common fluorescent excitation wavelengths like 488nm and 532nm, new markers are being continually developed, some of which have very unique excitation and emission wavelengths. In order for a flow cytometer system to be versatile, it needs to be able to accommodate as many unique sources as possible. However, as sources are added to the system it also means that an equal number of dichroic beam combining and separating filters is required as shown in Figure 6, the total cost of the filters required in the system can become exceedingly.

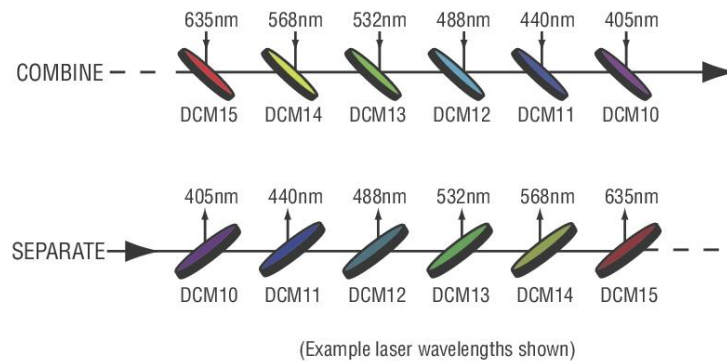


**Figure 6 - Example of Beam Combining & Separating:** diagram showing both a multi-filter beam combining path and a beam separator path [19].

Going back to the earlier question as to whether or not there are areas to drive cost out of the system, these beam combining filters would seem to offer an area to consider. What if a single lightpipe in conjunction with a focusing element is used as the combining elements for all of the sources in the system? Figure 7 show a simple version of what this type of system might look like. Here the dichroic beam combining filter is replaced the parabolic focusing mirror and tapered lightpipe. Now in the case where only two lasers are being used in the system the filters would likely be the cheaper solution. However, the benefit of this alternative approach is, with a broadband reflective coating applied to the parabolic mirror, additional sources can be added to the system without requiring any additional optics. Whereas the dichroic beam combining filters are wavelength and source specific, the parabolic reflector and tapered lightpipe are broadband optical components.

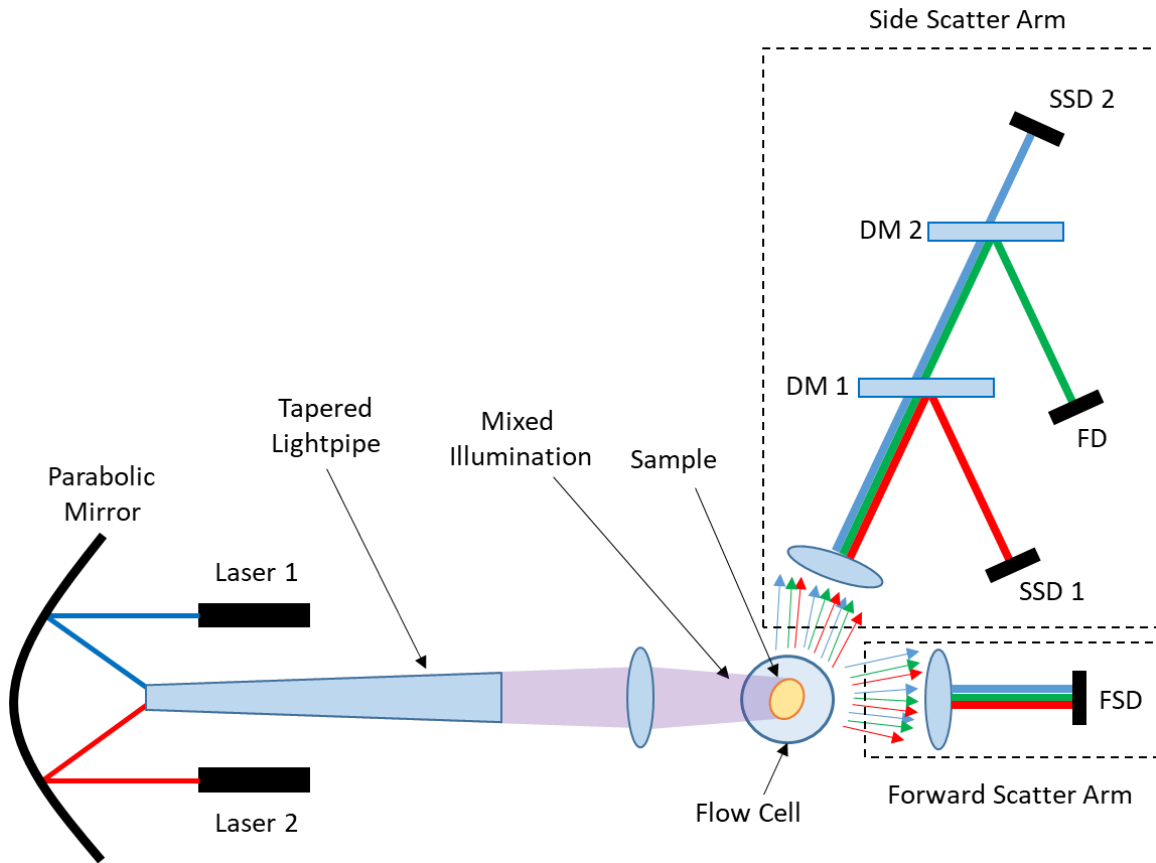


**Figure 7 – Flow Cytometer Layout Using a Lightpipe:** Similar diagram to Figure 4, however, the beam combining is done via a parabolic mirror and tapered lightpipe. This achieves beam combining and mixing at the same time.

The difficult part in taking this approach to integrating the sources is finding a lightpipe design that is cheap enough to offer the desired savings, while still offering sufficient performance for meeting the needs of the application. In such cases, if the number of input sources is only four then a simple square light pipe will be sufficient. However, this may not hold for a larger number of sources. For example, if there are six sources a hexagonal lightpipe will offer a better solution. In fact in cases where the number of sources is greater than six, research has shown that a lightpipe design which includes



specific sub-features along the sidewalls may be required in order to reach high levels of uniformity [1, 20]. However, before a more complex lightpipe design like this selected it is prudent to first confirm through testing that no other lightpipe solution is suitable given the increased degree of difficulty in manufacturing them. Determining where the cutoff is between each of these options, is crucial when looking to keep cost as low as possible, especially when the number of sources is low and therefore the cost to use a filter set is more manageable.

In this project, the aim was not to develop a solution for how to combine these sources, but rather to develop an inspection system for quantifying how effective possible solutions are to aid in this type of cost versus performance evaluation. Without the ability to measure the performance of proposed combining solutions, one cannot be sure if they are delivering on the required performance. Additionally, as is the case with most engineered devices, the goal is to reach a design which meets the requirements of the application, without overshooting the mark by a significant amount (typically illumination systems are budgeted with 25% safety factor) thereby adding unnecessary cost with an overdesigned solution. Also, once a design has been validated and deemed suitable for production, having a means to continue to inspect parts in production to ensure the anticipated performance is being maintained on a component level would be very beneficial. The inspection system detailed herein aims to provide the a solution for this type of proof-of-concept testing, while also offering a starting point for a more robust production testing system as well.

# Theory

## *Lightpipes, Uniformity, & Illumination Mixing Concepts*

Lightpipes are a key optical component in illumination system design. They are designed to guide light from a source to a target via reflections. While designs which use hollow reflective structures can be used, these components tend to be solid pieces of material that use total internal reflection (TIR). This is due to the fact that in theory TIR is more efficient than a mirror reflection which will have some loss due to the reflectivity being less than 100% [7]. Therefore in cases where a longer length rod is required the TIR based designs are preferred. Alternatively, hollow mirrored lightpipes will produce more reflections per unit length because they are working in air instead of glass and are easier to mount [7]. So in cases where a short lightpipe is required hollow mirrored lightpipes tend to be preferred. Primarily lightpipes have two main performance criteria, which are their ability to efficiently couple light from the source to the target and control of the distribution of the light output from the lightpipe. The testbed described herein focuses on testing the ability of various types of lightpipes in regards to the latter criterion by examining their ability to offer different types of uniformity in regards to the light distribution at their outputs.

In illumination there are various types of uniformity, which can essentially be divided into geometrical and spectral categories. Since this testbed is focused on the ability of the lightpipe to combine different individual narrow spectrum sources into one uniform, mixed output, we focus on the combination of these two categories through irradiance and

radiant intensity uniformities. Such can be done through either photometric or radiometric based quantities. We present both herein, since different applications require different unit considerations. Irradiance is a measure of the amount of light flux per unit area, or  $\text{W/m}^2$  [21]. Therefore if the lightpipe provides irradiance uniformity, the output is homogeneous spatially. Radiant intensity is a measure of the amount of light flux per unit solid angle, or  $\text{W/sr}$  [21]. Therefore if the lightpipe provides radiant intensity uniformity the output is homogeneous angularly.

The level of uniformity obtained at the output is a function of a few variables, namely the length of the lightpipe, the spatial distribution of the input light field, the angular distribution of the input light field, and the cross-sectional shape of the lightpipe [1]. In regards to spatial uniformity, ensuring that a sufficient number of reflections occur within the lightpipe is key. We can think of the lightpipe as a summation of subdivisions of the spatial distribution of the input beam, where the output is now a superposition of these inputs as shown in Figure 8 [1]. For a straight lightpipe the input angle of each ray and the width of the lightpipe will determine the number of reflections per unit length. Again looking at Figure 8 we can see that if the input angle entering the lightpipe were to be increased then the first reflection would occur sooner. Conversely if the input ray were to enter parallel to the axis of the lightpipe no reflections would occur. For thoroughness we must note that in the case of a solid lightpipe the input light will undergo refraction at the input face which will change the angle of reflection inside of the lightpipe slightly altering the number of reflection per unit length, however, for simplicity let us assume that there is no refraction at the input face.

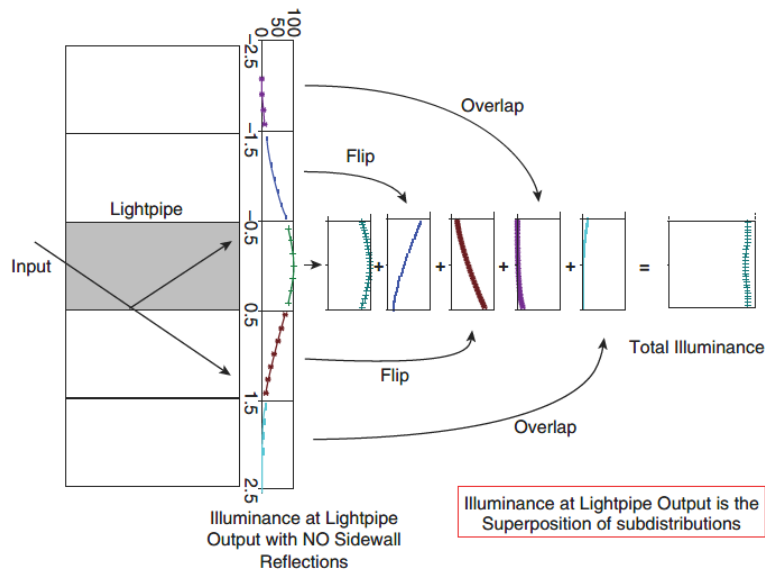


**Figure 8 – Lightpipe Illuminance Superposition:** Illustrates how the reflections within a lightpipe lead to the homogenization of the output, where the output is the summation of all the reflections in the lightpipe [1].

From there the length of the lightpipe will determine the total number of reflections and therefore the number of subdivisions that will make up the tunnel diagram for the lightpipe. If we take the spatial distribution at the output assuming there are no sidewalls and then overlay this with the representative tunnel diagram we can see that every replicated lightpipe in the tunnel diagram becomes a subdivision [22]. When summing these regions it is important to note if that subdivision corresponds to an even or odd number reflection. As you can see in Figure 8, the illuminance profile for an odd number reflection must be flipped about the axis of the lightpipe prior to summation. Those which correspond to even number reflections can be overlapped as-is and included in the summation. It has also been shown that the use of microstructures on the sidewalls of a lightpipe can act as a way of creating additional subdivisions and reducing the length of the

lightpipe needed to get the same amount of spatial uniformity [20] [23]. These is achieved by the microstructures leading to an increase in the number of reflections per unit length. Figure 9(i) shows an example of a typical square lightpipe and one which has a triangular microstructure applied to the sidewall. As we can see from the figure, a ray which is incident at one of the corners of the standard square lightpipe undergoes two reflections, while for the design which incorporates the triangular microstructure the number of reflections for the same input ray is doubled to 4.

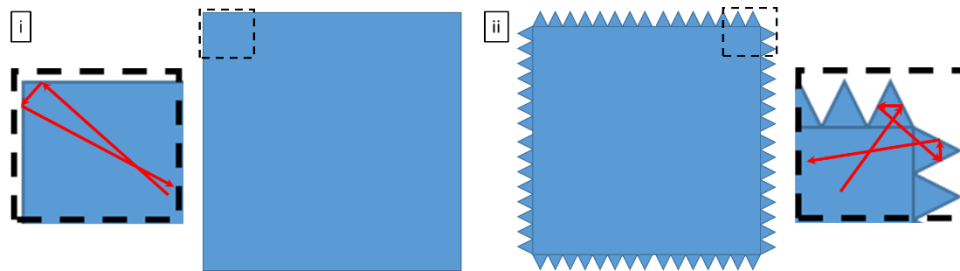


**Figure 9 – Square vs Square-Microstructured Lightpipe:** (i) shows a standard square lightpipe with a region of interest which illustrates what happens to rays which are incident on one of the corners of the lightpipe. Here this ray is reflected twice before exiting the corner. (ii) shows a square lightpipe which has a triangular microstructure applied to the sidewalls. The highlighted region of interest shows a similar ray incident on the corner of the lightpipe, however due to the microstructure this ray is reflected 4 times before exiting the corner [20].

In regards to angular uniformity, the same input parameters are main contributors to the output performance. However the use of a tapered lightpipe provides an additional way to increase angular uniformity. Additionally, adding the type microstructures

previously shown in Figure 9 (ii) to a lightpipe design which already offers good angular uniformity can again serve as a means of increasing the spatial uniformity of lightpipes by increasing the number of reflections per unit length [20]. Uniformity in both spatial and angular spaces is the key to controlling the color mixing when using multiple individual color inputs [20]. It has been shown that the alignment of the lightpipe spatially with respect to the input source(s) also has a great effect on the uniformity [1]. For example it has been shown that a decenter between the two can create a gradient in the illuminance of the output and discontinuities in the intensity distribution of the output [1].

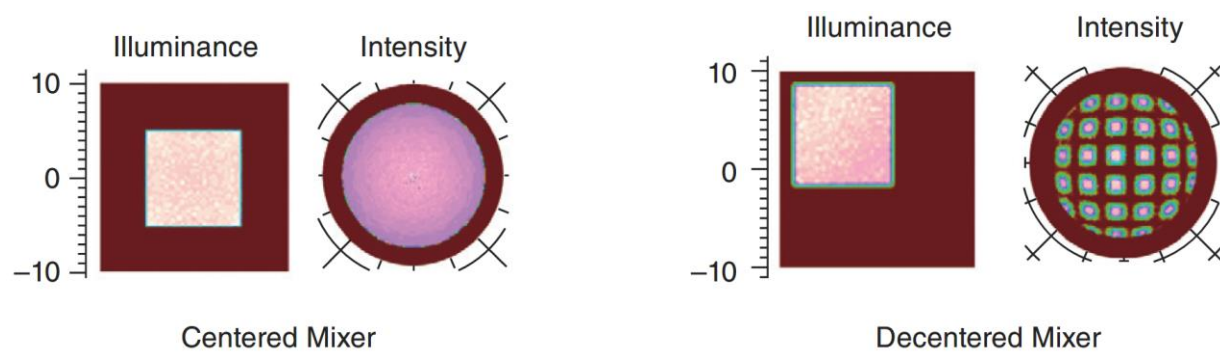


**Figure 10 – Effects of a Decenter Lightpipe:** Figure show the Illuminance and Intensity existing a square lightpipe when the lightpipe is centered (left) with respect to the light source and when it is decentered (right) with respect to the light source. In the case of the centered lightpipe both distributions are uniformity, however, in the case of the decentered lightpipe the illuminance has a slight gradient and the intensity distribution has discontinuities [1].

This is something to be considered in the system design when using a lightpipe, and for the purposes of this discussion needs to be considered in the design of our testbed. The

accuracy of the alignment of the lightpipe to the input field must be such that it does not influence the quality of our measurement. For a bolt together testbed it must be shown that the tolerance of this alignment is less than the amount of decenter that creates an illuminance gradient or discontinuous intensity profile. Alternatively the mechanical design may include a degree of freedom to actively align the lightpipe with respect to the light source to ensure this optimal performance.

If coherent sources are to be used then there are additional concerns that must be considered. For the purposes of the applications we have been discussing the effects of spatial coherence, in particular, are concerning. In the case of the laser sources which are used in the applications discussed earlier, spatial coherence arises from the superposition of light and the fact that these light sources have a finite spatial extent. For example if we have two waves emitting from the two separate points along our extended source they will ultimately overlap in space [24]. The amount of spatial separation between where these two waves emanate from along the source and their ability to stay in phase with one another over a given distance they are propagate will determine how much they interfere with one another.

This interference manifests itself in a fringe pattern at the target area due to the interference between the two. In a coherent beam the different regions of the beam are essentially propagating in space in phase [25]. When looking to create a uniform illuminated area as we are for the two application spacing discussed earlier, having this type of fringe pattern arise at the target area is not ideal; therefore, ways to break up the phase of the coherent beam need to be explored.

One way to address this is to use a solid lightpipe where the coherent input is focused into the entrance face of the lightpipe as described in Figure 7, and ensuring there are a large number of TIR events prior to light exiting the lightpipe. TIR will induce an angle of incidence (AOI) dependent phase delay to the rays within the beam, where the converging input will create a distribution of AOIs within population of rays [24, 26]. This will ensure there is a sufficient number of reflections so that the optical path length of the beam exiting the lightpipe is greater than the coherence length of the source, and that there is a distribution of AOIs within the ray populations due to the converging input beam, mitigating the coherence of the input.

The number of reflections within the lightpipe not only impacts the output spatial uniformity, it is also important, when coherent sources are used, to minimize speckle effects [27]. If the accumulated effect of TIR events within the lightpipe are not sufficient to fully break down the source coherence an external device, such as a rotating holographic diffuser, can be added to more fully break up the beam. This is not a preferred approach as it introduces not only extra cost and complexity, it also reduces efficiency and add additional vibration into the system.

### ***Integrating Spheres***

An integrating sphere is an optical device which can provide a uniform light source. For the purposes of this study we will use the integrating sphere as uniformity standard to determine the level of uncertainty in the measurements from the testbed. The basic design is rather simple as, in theory, this is a hollow spherical device with the inside coated with a Lambertian material so that ultimately the radiance on the inner surface is independent of



angle. Since the interior of the sphere is Lambertian all of the internal reflections can be integrated over for a single area element  $dA$ .

The irradiance over the sphere is constant in theory, however, in practice this is not the case. The Lambertian coating material on the interior will not be a perfect reflector, and the input and output ports create discontinuities in the sphere which also degrade the uniformity. With this in mind the ratio of the port area to the size of the sphere must be considered with the following equation offering a useful guideline:

$$L = \frac{\rho\Phi}{\pi A_{sphere}[1-\rho(1-f)]} \quad (3)$$

Where  $f$  is the ratio of the total port area to that of the sphere,  $\rho$  is the reflectance of the inner coating, and  $\Phi$  is the radiant power of the source.

### ***Bidirectional Reflectance Distribution Function (BRDF)***

In flow cytometry where there will be a wide range of possible cell geometries, we must use the fundamental geometric descriptor of reflectance which is the bidirectional reflectance distribution function (BRDF) [28]. The BRDF is equal to:

$$BRDF(\theta_i, \phi_i; \theta_r, \phi_r) = \frac{L(\theta_r, \phi_r)}{E(\theta_i, \phi_i)} \quad (4)$$

where  $L$  is the reflected radiance of the cell surface and  $E$  is the incident irradiance of the surface. In cases where the flow cytometer system uses a collimated beam for its illumination this relationship is straightforward, however, seeing that most system use a converging beam there is still more we must consider. Figure 11 illustrates this by first showing what occurs when the input beam is perfectly collimated (Fig. 11i), without any

divergence or convergence, and all of rays having the same angle. The angle of reflection of each ray is varied only due to the geometry of the cell, and if the incident beam was spatially uniform the bidirectional reflectance distribution function (BRDF) observed by the SCD is purely due to the surface of the cell as expected.

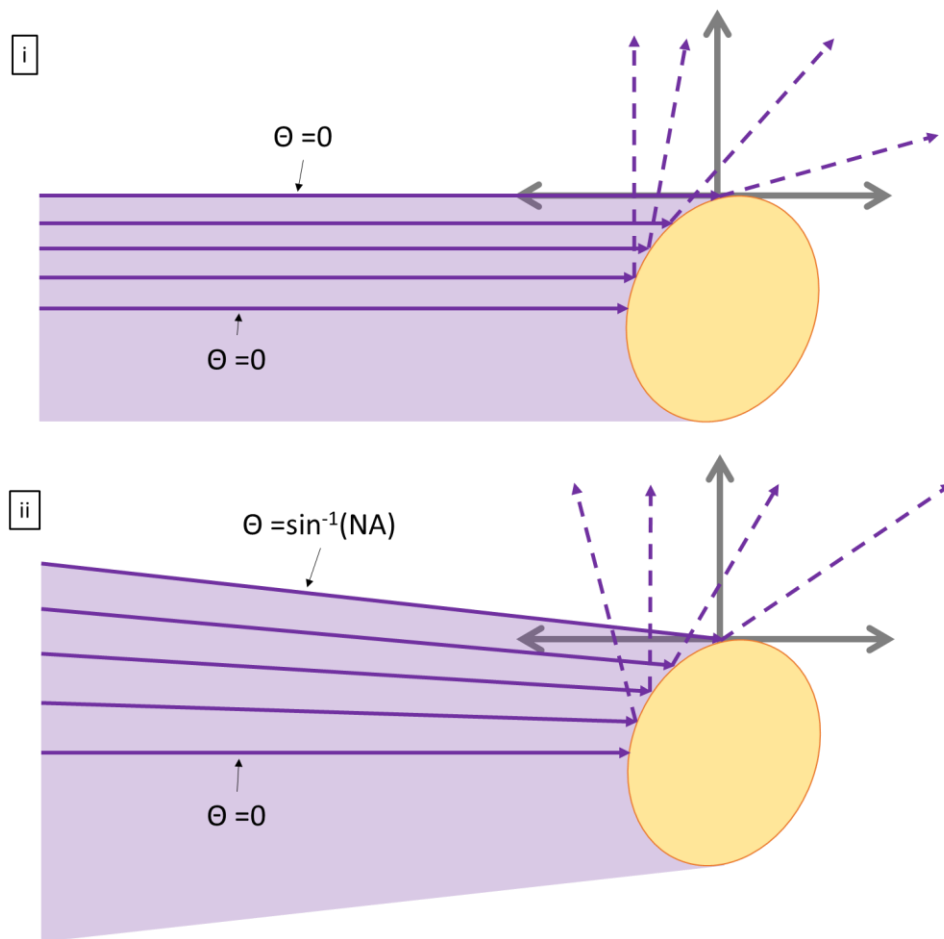


**Figure 11 –Collimated vs Converging Cellular Excitation Beam:** Illustrates the effect of having a collimated or converging input beam. (i) Shows a collimated input beam where the angles at which each ray are reflected is due to the surface of the cell. (ii) Shows converging input beam where the angles at which each ray are reflected is due to both the surface of the cell and the input angle of each ray.

However, system which use a converging beam are slightly more complex than this. Figure 11(ii) illustrates what happens when a converging beam is used. Here there is a range of angles within the beam which corresponds to its NA, which means there will be a variance in the illumination angle observed by different regions of the cell. The BRDF is then a function of the geometry of the cell surface and the NA of the converging input beam. Furthermore, while having a spatially uniform input beam is still important, it must be angularly uniform as well. For instance if the beam in Figure 11ii has a higher radiant intensity at  $\theta = 0$  than it does at  $\theta = \sin^{-1}(\text{NA})$  the BRDF measured will no longer only be a function of the cell surface. Therefore in order to provide the highest fidelity measurement of the BRDF with a converging beam, angular uniformity of the input beam is required.

### ***System Architecture Options***

The solution space in regards to system architecture options for illumination uniformity test systems is rather rich. In fact there are two main categories from which to choose. The first are those which are simpler optically and more demanding mechanically to implement. This includes various designs where a radiometer is coupled to a series of stages to scan the illumination area or field. These radiometers can be as simple as a bare detector when being used to measure the uniformity of an area. The angular field of view in this case is  $\sim 180$ . A slightly more sophisticated radiometer design would introduce an aperture in front of the detector. This offers the ability to tune the angular field of view of the radiometer based on the distance between the aperture stop and the detector, and the

size of the detector. Baffles can also be incorporated to reduce stray light and increase the signal to noise ratio of the radiometer.

For measuring angular uniformity it is ideal to limit the angular field of view as much as possible. This can be done by simply increasing the spacing between the aperture and the detector to great length, however, in practice this can make the implementation of stage system much tougher. This will add length and weight to the radiometer which then needs to be scanned to sample the full angle range which is intended to be measured. An alternative option is to introduce a lens in front of the aperture. With the aperture placed at the back focal plane of the lens it will act as a spatial filter which is centered with respect to the lens. Only collimated light coming into the lens will make through the spatial filter. Now the radiometer only measures on-axis light, and in a much smaller and lighter package.

In either case the performance of the radiometer itself is going to be mainly limited by the centration of the detector and the aperture, and in the case where the lens is used the centration of the lens as well. To accurately assess the boresight error of the radiometer an RSS tolerance analysis should be performed. In the case where a relative uniformity measure is sufficient then these alignment errors do not necessarily need to be eliminated, rather kept consistent across the data acquisition. That is to say that if for instance there is a slight decenter of the aperture with respect to the collection lens, while the measurement may not be of the on-axis light as long as this misalignment is consistent in all measurements obtained across the angular range scanned by the radiometer a relative uniformity value can still be accurately obtained.

One of the major benefits of this type of system beyond the simplicity of the optical design is the level of light sensitivity that can be obtained with regards to the detector. Here

only a single detector element is required which allows for easy tailoring of the electronics to yield a high dynamic range of measurement. A simple silicon detector coupled with a low-noise amplifier circuit and high resolution ammeter can offer a high degree of sensitivity. Particularly for situations where the amount of light is fairly low this can be of great benefit.

The main limiting factor of these types of system will ultimately come down to the positioning system. The accuracy, repeatability, and speed of the positioning system used to scan the radiometer is going to dominate the system performance. As the spatial irradiance and angular intensity maps are being built point-by-point, the level of fidelity in the positioning of said points is critical. In the case where a single 1D slice only need to be obtained the step accuracy of the positioning system is going to limit the uncertainty of the data. When raster scanning to create a 2D map the repeatability of the stages in the positioning system will also add further uncertainty to the data. In either case the speed with which the positioning system can scan, and the detector can capture the data can also limit the accuracy. If the cycle time of the scan is rather long it can become difficult to decouple variance in the mixing of the optic under test from variances in the light source over time.

The second category of systems uses higher performance optical solutions to alleviate the mechanical demands of the type of radiometer scanning systems mentioned previously. Generally these will use a 2D detector array rather than the type of single point detector mentioned previously. Here the optics are used to collect light over the entire area or angular field within a single image. In regards to measuring the irradiance of an area over a given angular range, a standard imaging system can accomplish this, the caveat is

going to be make sure that the system is collecting light over the angular range of the mixing optic that is under test. The object space numerical aperture of the optics must be such that it covers the angular range of the output of the lightpipe. Otherwise any effect of angular non-uniformities beyond the numerical aperture of the imaging system are not being taken into account.

While limited in the area over which they can image, a microscope objective and tube length system can offer a very high numerical aperture imaging system. Here the magnification of the system, and therefore the area imaged for a given detector array size, is going to be set by the ratio of the effective focal length of the tube lens and objective. For example Nikon designs all of their objectives to be used with a 200mm effective focal length tube lens, where their 20X apochromatic objective offers a 0.55 numerical aperture with a 10mm effective focal length. When used with a 1" format camera sensor the area being captured in the image is only 256 $\mu$ m x 192 $\mu$ m. However, this can be increased slightly by substituting a shorter focal length tube lens into the system. If a 40mm effective focal length lens is used as the tube lens in the system the magnification is decreased to 10X. This will increase the area being imaged to 1.28mm x 0.96mm, while still maintaining the object space numerical aperture of 0.55. Since a detector array is being used if that area is sufficient for testing no scanning system is needed.

In regards to imaging systems that can capture a full angular data set in a single image there are a few options as well. The first is that of a conoscope, where an aperture is placed one focal length in front of the lens and the detector is placed one focal length behind. This yields an image of the angular field on the detector. A design using off-the-shelf optics is desired, but a solution maintaining a flat MTF response across the image is

not readily available. A similar setup can be achieved using an eyepiece in reverse. Here the aperture stop is placed at the eye relief, and the detector is placed where the intermediate image would typically be. The compromises here can again be resolution roll off over the image, and the angular field of view. As the angular field of view is increased the roll off in the MTF over the field typically will increase as well. Most high end wide field of view eyepieces will still only offer up to  $\pm 20$  degree field of view, and carry with them quite a bit of contrast drop from on-axis to full-field.

In cases where a large field of view is needed a hypercentric lens can be a viable alternative. These lenses provide a converging view emanating from a virtual convergence point. Where an object space telecentric lens will have a front group with a rear focal point which is coincident with the aperture stop of the system and chief ray angle of zero in image space, a hypercentric lens is going to have a front group which is two focal lengths away from the aperture stop in the system and a negative chief ray angle in image space. These tend to be used for machine vision applications like bottle inspection where it allows the top and side of the object to be imaged at the same time. Figure 12 provides a diagram which illustrates in more detail how the lens works [29].

In Figure 12 to left is a schematic of the front of the lens which details all of important parameters for operating the lens. The first of these are the convergence point (CP) and maximum viewing angle (MVA). The CP is where all of the rays collected by the lens appear to emanate from, this is the virtual convergence point mentioned earlier which is two focal lengths away from the front group (the convergence point distance or CPD is the distance from the front of the lens to this convergence point). Next there is the near viewing cone (NVC) which defines the volume within which objects should be placed

for optimal imaging performance. The near aperture (T) and far aperture (B) of the NVC are also noted, where the distance between them defines the maximum working distance (MaxWD). Here the working distance is defined by the distance from the front of the lens to the top of the object.

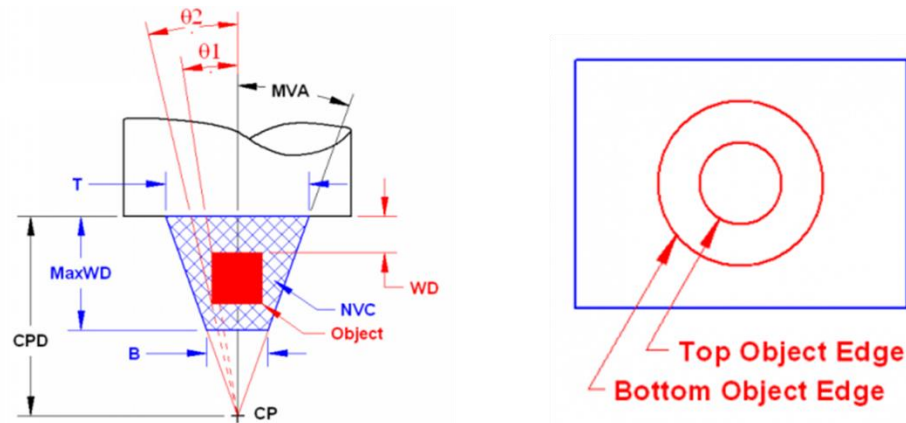


**Figure 12- Hypercentric Lens Diagram & Example Image:** To the left we have a simple diagram of the front of a hypercentric lens. This shows a cylindrical object which is positioned within the Near Viewing Cone (NVC). To the right we have the image which is obtained using this type of lens where the top and bottom edge of this object are then displayed concentric to one another due to the nature of the lens. Here the top of the object maps toward the center of the image while the bottom edge of the object maps towards the edge of the image [29].

Last, and likely most important angle  $\theta_1$  and  $\theta_2$  are defined.  $\theta_1$  is the angle between the optical axis of the lens and the line of intersection between the CP and the top object edge.  $\theta_2$  is the angle between the optical axis of the lens and the line of intersection between the CP and the bottom object edge. These are important when interpreting the



image obtained by the lens represented by the image to the right in Figure 12. In the image we see two concentric circles corresponding to the top object edge and bottom object edge, with the radius of each circle equal to  $\theta_1$  and  $\theta_2$  respectively.

This viewing angle to image mapping will be important to remember later when reviewing the lightpipe output angular uniformity data collected with the hypercentric lens. There the lens will take the output field and convert it into a similar polar coordinate map of the light field. When stopped down to  $f/16$  this lens offers diffraction limited imaging performance across the field, while limiting the angular subtense associated to each pixel. Also, when using a hypercentric lens to measure the angular uniformity of the output of a lightpipe the exit face of the light pipe should be within the specified NVC of the lens for optimal performance.

# Materials and Methods

## *Point-by-Point Scanning Collection Systems*

From an optical perspective the radiometer based system is rather simple. In this optical system an uncoated UV fused silica PCX lens (#48-028, Edmund Optics, Inc., Barrington, NJ, USA) operating at  $f/10$  is used to focus a planar wavefront entering the radiometer through 20  $\mu\text{m}$  aperture (#56-279, Edmund Optics, Inc., Barrington, NJ, USA). The aperture is placed at the focal point of the lens to act as a spatial filter which only allows the on-axis rays entering the lens to pass through to the detector (OSI Optoelectronics, Montreal, QC, Canada). Setting this distance is achieved by mounting the lens in a simple thin lens mount (#54-615, Edmund Optics, Inc., Barrington, NJ, USA) coupled with a fine thread focus tube (#03-625, Edmund Optics, Inc., Barrington, NJ, USA) and a 50-mm extension tube allows for the focal distance to be zeroed out.

Additionally, if the aperture mount is modified to include three through-holes 120 degrees apart for set screws, the centration of the aperture with respect to the lens can be zeroed out as well. This design offers sub arcminute angular field selectivity, which was verified through tolerance analysis. ZEMAX optical design software (Kirkland, Washington, USA) was used to analyze the tolerances of the lens itself, along with the tolerances of the mechanics which were not actively zeroed out. For these, Monte Carlo simulations with the following tolerances applied were run.

<b><u>Lens Tolerances</u></b> <ul style="list-style-type: none"> <li>- Test plate radii: 0.1%</li> <li>- Power: 3 Fringes at 633nm</li> <li>- Irregularity: 0.5 Fringes at 633nm</li> <li>- Beam Deviation: 1 arcmin (0.0367 degree wedge)</li> <li>- Center Thickness: +/- 50um</li> <li>- Index: +/- 0.001</li> <li>- Abbe: +/- 1%</li> <li>- Outer Diameter Tolerance: +/-25um</li> </ul>	<b><u>Lens Mount Tolerances</u></b> <ul style="list-style-type: none"> <li>- Seat Tilt: +/- 0.25 degrees</li> <li>- Bore Inner Diameter: +25um/-0</li> <li>- Bore Concentricity: +/- 20um</li> </ul> <b><u>Compensator</u></b> <ul style="list-style-type: none"> <li>- Z distance to the detector plane set as a compensator based on the use of the fine focus ring to actively zero out the position of the aperture.</li> </ul>
--	--

**Table 1 - PCX Lens Radiometer Tolerance Table:** List of tolerances entered into Monte Carlo simulation to predict the spot size performance of the radiometer. Tolerances are based on those of the catalog parts selected for this device. The compensator is implemented based on the design of the mechanics discussed earlier, and planned assembly method.

The perturbed Monte Carlo lenses were then evaluated for RMS spot size. 500 Monte Carlo simulations were run based on a normal distribution of the tolerances, with the anticipated yield percentage captured at various RMS spot sizes. From this an estimated peak-to-valley (PV) spot size was also derived based on the approximation that the PV values is generally 5 times that of the RMS value. Below is a table showing these results. Based on these results the radiometer system will be able to provide a spot size of less than 20um in order to achieve sub-arcminute resolution.

<b>Yield Percentage</b>	<b>RMS Spot Size (um)</b>	<b>Estimated PV Spot Size (um)</b>
98% >	1.518	7.590
90% >	1.439	7.195
80% >	1.394	6.970
50% >	1.325	6.625
20% >	1.252	6.260
10% >	1.216	6.080
2%>	1.144	5.720

**Table 2 - Radiometer Yield Results:** This table shows the model yield from the Monte Carlo simulations based on the tolerances in Table 1. Based on these results the modeled RMS spot size is well within the diameter of the 10um aperture stop needed for spatial filtering, and our estimated PV spot size is as well.

For testing the spatial uniformity a similar scanning system was developed. In this case however, rather than using a PCX lens, a microscope objective was used, and rather than have the aperture in image space the aperture was place in front of the lens in object space. In this system the aperture sets the spatial area light is collected over for a single point. The objective was selected to have an NA of 0.55 to ensure the ability collect light beyond a 30 degree input angle, which was based on the coherent system which will be discussed in more detail later. While it is true that a radiometer system with a simple aperture and detector could have been used, this would require far more accuracy in the alignment of the aperture with respect to the detector. Any misalignment of the two would affect the sampling. With the objective based system if the aperture is slightly misaligned

the result is the magnified image of the aperture will be laterally displaced at the image plane. In this case, the detector is not acting as a field stop so it can be slightly oversized to compensate for this.

In either of the radiometers we just discussed it is important to realize that the resolutions noted for each were only for a single measurement or point in space. When measuring either the spatial or angular uniformity of the output of a lightpipe an entire point cloud will need to be collected by scanning each radiometer. Ultimately the resolution of the point cloud, and therefore the uniformity measurements, will then be limited by the stages used for scanning. For cost considerations off the shelf linear and rotary stages from Zaber Technologies Inc. (Vancouver, BC, CA) were selected for this initial evaluation. These units did not contain encoders. The stages were controlled through a custom LabView (National Instruments, Austin, TX, USA) program which contained the scanning routine. Figure 13(i) and 13(ii) show the basic layout of each of these systems.

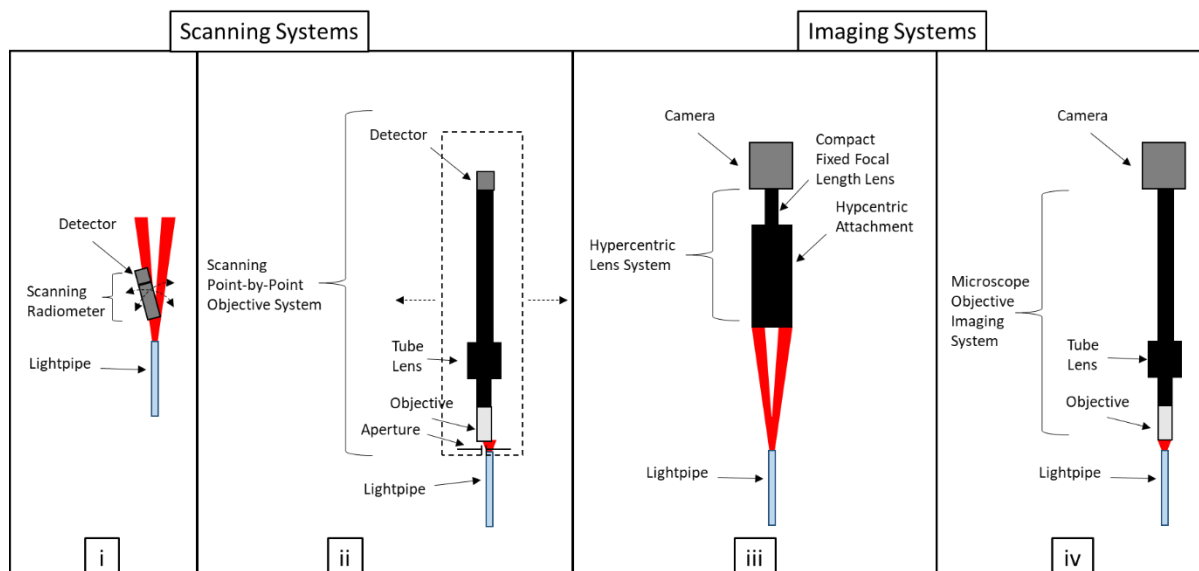


**Figure 13 - Scanning & Imaging System Layouts:** (i) Shows the point-by-point scanning PCX radiometer system for measuring angular uniformity. (ii) Shows the point-by-point scanning objective radiometer system for measuring spatial uniformity. (iii) Shows the hypercentric imaging system for measuring angular uniformity. (iv) Shows microscope objective system for measuring spatial uniformity.

### ***Detector Array & Imaging Based Collection Systems***

Based on the sub-micron spatial resolution required to validate the irradiance uniformity for lightpipes being used in a flow cytometer a high magnification objective system was used as shown in Figure 13(iii). Typically CMOS sensors containing pixels that are smaller than 4-5 $\mu$ m tend to be somewhat noisy, so the EO-1312 Monochrome USB 3.0 camera (Edmund Optics, Inc., Barrington, NJ, USA) which has an e2v EV76C560BB sensor containing 5.3 $\mu$ m pixels was selected for the testbed. In order to sample down to 0.2 $\mu$ m or smaller with this sensor a microscope objective offering 26.5X or greater is required. However, as the magnification increases the captured field of view in each image will decrease. In order to balance these constraints among the available off-the-shelf objective options (NA, magnification, designed tube lens EFL, etc.), a 20X 0.75 NA CFI Plan apochromatic microscope objective from Nikon (Nikon Instruments, Inc., Melville, NY, USA) was selected for this initial iteration. This objective is design to be used with a 200mm EFL tube lens. For ease of mounting a 200mm EFL tube lens from Mitutoyo (MT-1, Mitutoyo Corporation, Kanagawa, Japan) was used. Also, while this detector and objective lens system can be used to form a scanning spatial sampling subsystem to increase the area capture, for this initial version a scanning motor system was not implemented.

For measuring the angular uniformity the same general system layout was used as shown in Figure 13(iv), however the microscope objective imaging system was replaced with a hypercentric imaging system (#86-586, Edmund Optics, Inc. Barrington, NJ, USA; Light Works, LLC, Toledo, OH, USA). This specific hypercentric lens offers a maximum viewing angle of 33 degrees. For more information on the performance of the hypercentric lens please see APPENDIX A.

### ***Incoherent Illumination System for Uncertainty Determination***

A 4" general purpose integrating sphere from Labsphere, Inc. (3P-GPS-040-SF, North Sutton, NH, USA) was used as the uniform illumination source for determining the level of uncertainty in these measurement systems. The inner surface of this integrating sphere is coated with their Spectralect® Diffuse Reflectance Coating which provides a near Lambertian reflective surface for the interior of the integrating sphere. This was paired with a Dolan-Jenner DC-950H fiber optic illuminator (Setra Systems, Inc., Boxborough, MA, USA) to provide a stable (< 0.5% variation in output power) incoherent illumination source. The two were coupled to one another via a flexible fiber optic light guide (#42-344, Edmund Optics, Inc., Barrington, NJ, USA).

### ***Coherent Illumination System for Testing***

For the purposes of testing each lightpipe's ability to breakdown the coherence of an input source, a highly coherent source was required. For this reason a helium-neon laser from JDSU (#1508-1, Lumentum Operations LLC, Milpitas, CA, USA) was used as the coherent source with a coherence length of greater than 25cm. In order to provide the

ability to adjust the beam diameter this laser was coupled to a 2X-8X variable beam expander (#87-569, Edmund Optics, Inc., Barrington, NJ, USA). This was paired with a focusing optic allowing for the ability to vary the numerical aperture of the illumination going into the lightpipe under test as show in Figure 14.

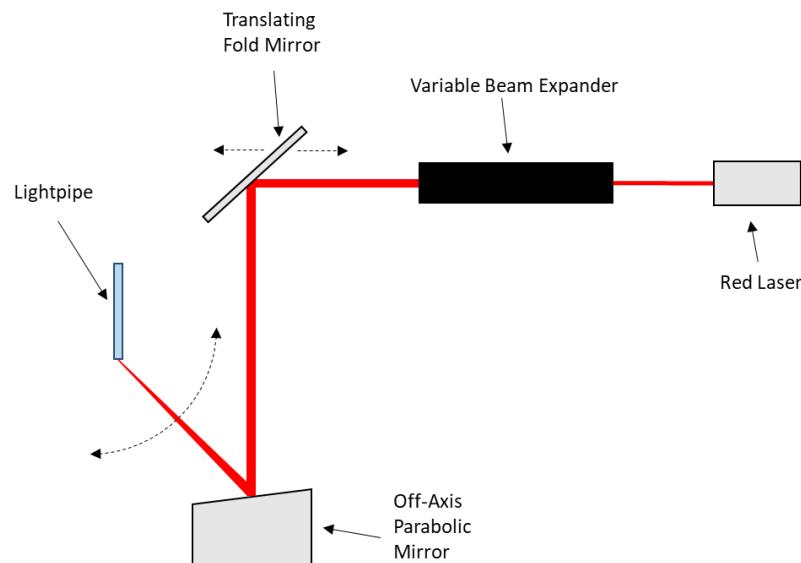


**Figure 14 – Coherent Illumination Layout:** Shows the coherent source, which is a HeNe laser, and the 2 variable elements to the input illumination setup. The first adjustable piece in the system is the variable beam expander which adjusts the beam diameter incident on the off-axis parabolic mirror and therefore the NA of the input light. The second is the translating fold mirror which adjusts the position of the beam on the off-axis parabolic mirror. This slightly shifts the input angle of the gut ray within the input NA.

For this design an off-axis parabolic (OAP) focusing mirror was used as the focusing optic in the system. With a maximum viewing angle of the hypercentric lens of 33 degrees,



a 30 degree OAP (#47-089, Edmund Optics, Inc., Barrington, NJ, USA) was used in this particular version. Using an OAP as the focusing optic has the advantage of offering the ability to vary the input angle. Small changes in the gut ray angle of the input beam reflecting off of the mirror can be created by simply laterally shifting the beam with respect to the mirror as indicated in Figure 14. In order to achieve this a fold mirror was attached to a crossed-roller bearing single axis stage (#66-415, Edmund Optics, Inc., Barrington, NJ, USA). A kinematic mirror mount (#58-853, Edmund Optics, Inc., Barrington, NJ, USA) was also used to hold the mirror and provide the degrees of freedom necessary to align the input beam properly with respect to the OAP.

### ***Image and Data Analysis***

All of the image processing and initial data analysis was done in Matlab. Image processing algorithms were used during the initial setup of the imaging systems to verify the alignment of the imaging optics with respect to the lightpipe under test, as well as perform more advanced calculations and analysis on all 2D data set collected with each system type. For the angular uniformity data analysis Matlab was used to convert the captured image from a polar coordinate system in terms of radius ( $R$ ) and theta ( $\theta$ ), to an “unwrapped”  $R \times \theta$  image. This allows for specific  $\theta$  bandwidths to be isolated for analysis, which is very useful as there will be specific bandwidths of interest based on the NA of our input illumination. The Figure 15 below shows the change in mapping that is created via this process.

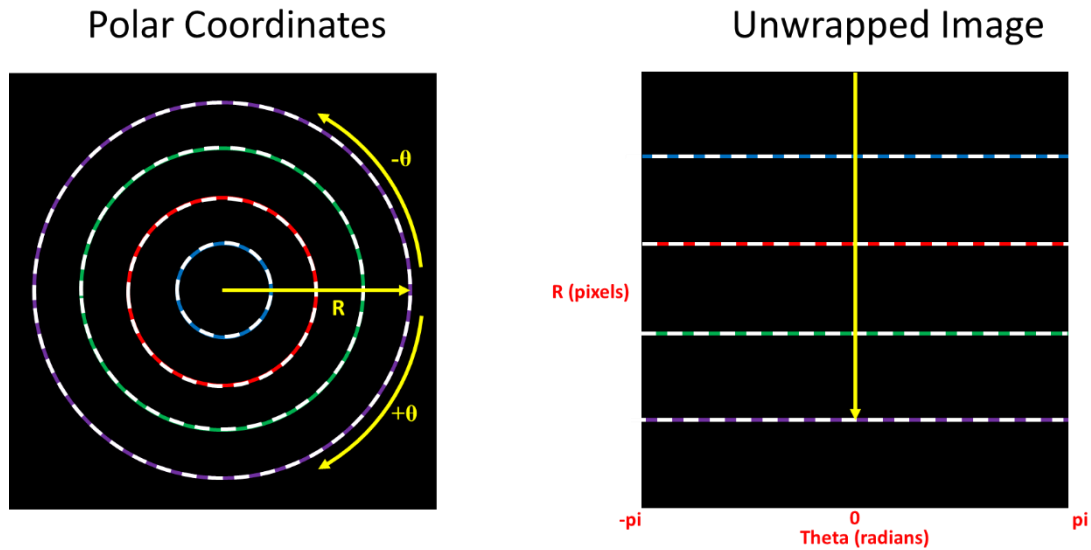


**Figure 15 – “Unwrapping” the Polar Image:** This shows the conversion in the pixel mapping from the polar image to the “unwrapped” version. Note the color of the rings from center to edge in the polar image and how these map top to bottom respectively in the “unwrapped” image. Also, note the yellow arrow which indicates the direction of  $R$  in both images, while also providing a reference to the  $\theta = 0$  in both images.

Here the “unwrapped” image shows the rings in the polar image as straight lines. The rings toward the center of the polar image are now represented by straight lines at the top of the “unwrapped” image, with the yellow arrow from the polar image also mapped over to provide a reference for  $\theta = 0$ . Figure 16 shows an example of a simple image going through this conversion, where the pixilation of the image manifest itself as ripples in the “unwrapped” image due to the subpixel interpolation of the unwrapping algorithm. This will be important to remember later on when we consider the uncertainty of the system/algorithm.

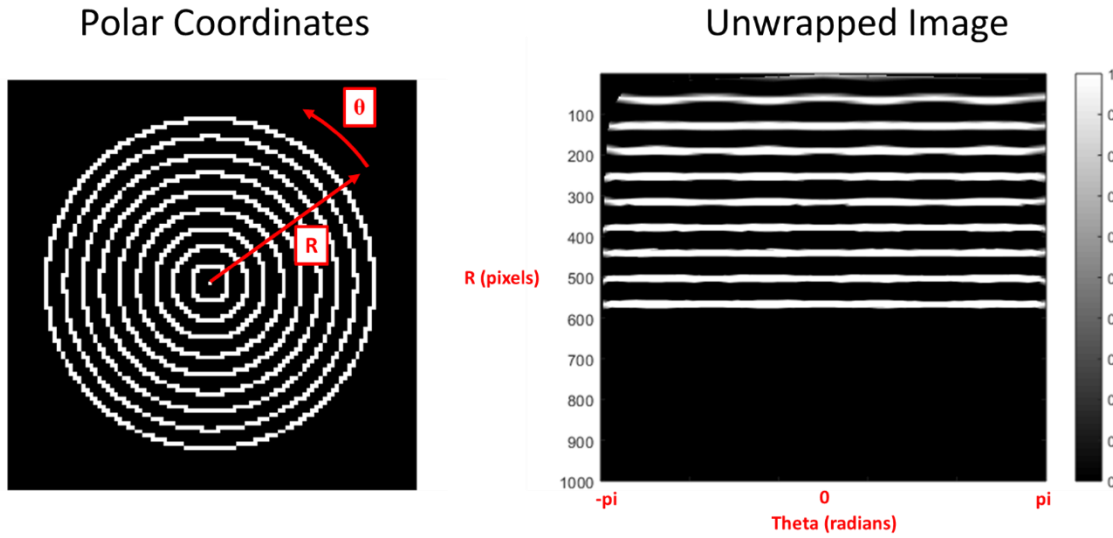


**Figure 16 – Pixelated Example of “Unwrapping”:** This figure shows how the pixelated edges of the polar image can manifest themselves as wavy edges in the unwrapped image.

The coefficient of variation (CV) was selected as the metric for quantifying uniformity of the irradiance and radiant intensity profiles. The coefficient of variation was calculated based on the following equation:

$$CV = \frac{\sigma}{\mu} \quad (5)$$

Where  $\sigma$  is the standard deviation of the 2D intensity or irradiance and  $\mu$  is the mean of the 2D intensity or irradiance.

As an additional metric for analyzing the spatial uniformity data the power spectral density (PSD) of the image was calculated as well. This was used as a metric to detect the presence of coherence in the irradiance profile, as the PSD will highlight spatial frequencies where there is periodicity in the irradiance profile.

The PSD of the irradiance profile ( $I_{2D}$ ) was calculated based on the following equation:

$$PSD = \frac{1}{A} * F[I_{2D}]^2 \quad (6)$$

Where the Fourier transform of the 2D irradiance profile is squared and normalized by A, which is the area of the image.

# System Comparison & Selection

## *Review of System Tradeoffs*

While in theory both the point-by-point radiometric systems and the detector array based imaging systems offer the ability to evaluate both angular and spatial uniformity, in practice each has their own benefits and drawbacks. When using top of the line equipment and in instances where the cycle time of the measurement is not critical the point-by-point type system is ideal. This will offer the greatest light sensitivity and overall performance when supported with the right electronics (high resolution ammeter, low noise power source, etc.) and motion system (high step resolution, high repeatability stages with encoders, etc.). Here the optical solution can be simple and cost effective, but the electronics and motion system can prove very costly in order to drive down the uncertainty level of the system and therefore yield the high fidelity measurement desired. Without this, not only is there uncertainty in the depth of the light level measurement, but also in the positional accuracy of the individual points in the final data cloud.

The imaging based systems are much simpler. Here since a two dimensional image is being capture the stages are much simpler as they are only required for the initial setup and alignment of the lens system with respect to the lightpipe. There are no concerns about the positional uncertainty of the pixels only of the alignment of the system with respect to the lightpipe under test, which in fact is also a concern in the point-by-point systems. The tradeoff here however is in the light sensitivity. The dynamic range of a typical detector array will not match that of a high end radiometer. So in cases where light levels may be

quite low the point-by-point system is likely still the better option. However, if light levels are not a concern, the imaging based systems are much more straightforward to implement and more cost effective.

### ***Angular Uniformity Noise Determination & Comparison***

In order to quantify the noise level in these two system types with the actual hardware implemented for this initial study, both systems were used to measure the output of a uniform standard. In this instance an integrating sphere was used to serve as this uniform standard as these provide angular and spatial uniformity. This was coupled to an incoherent source as described earlier to ensure that there were no coherence effects present in the noise level measurement. Figure 17 shows the full setup used for determining the noise levels of both the radiometer (i) and camera based (ii) angular uniformity measurement systems.

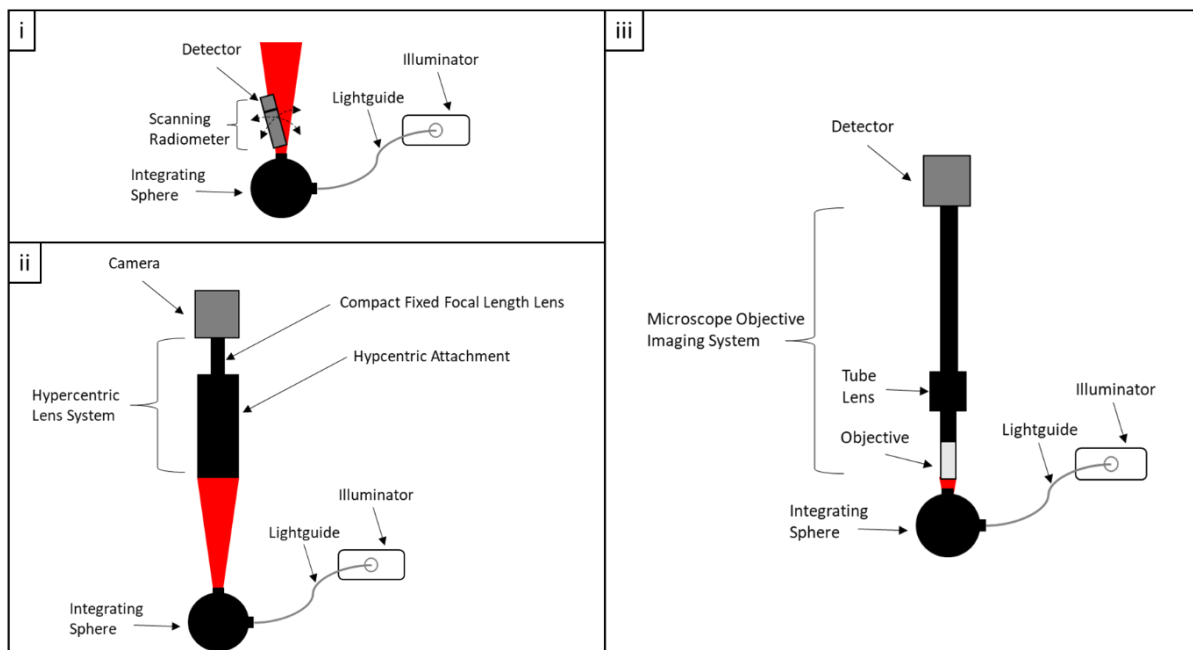


**Figure 17 – Layouts for Determining Noise Levels:** (i) Shows an incoherent illuminator coupled to an integrating sphere via a fiber optic lightguide to provide a spatially and angularly uniform source for determining the noise level of the point-by-point scanning radiometer system for angular uniformity. (ii) Shows the same illumination system but used for determining the noise level of the hypercentric imaging system for angular uniformity testing. (iii) Shows the same illumination system but used for determining the noise level of the microscope objective imaging system for spatial uniformity testing

Upon reviewing the data collected with each system it is clear that the imaging based system utilizing the hypercentric imaging lens was far superior. Assuming the output of the integrating sphere is uniform based on its design the noise level of each system was calculated by determining the resulting CV for each resulting data set. The results were rather striking as the hypercentric system offered a CV value of 0.0018 while the scanning radiometer system offered a value of 0.2715, a difference of greater than two orders of magnitude. This will also be discussed in more detail when reviewing the data collected in the experimental section where two different types of lightpipe are evaluated, however, it is worth noting now that the resulting CV values in that case study range from ~0.1-0.7. So while in the case of the hypercentric system the resulting uncertainty level would be around 1%, the scanning radiometer has essentially 100% uncertainty.

Figure 18 shows a comparison of the two data sets captured with each system. It is worth reiterating that the high level of uncertainty in the scanning radiometer system as constructed for this initial iteration is due to a limitation in the subcomponents used. The

repeatability in the position of the motorized stages and the noise of the electronics used for this specific embodiment were the limiting factor. With further investment into higher precision components, specifically the addition of encoders, there is no reason the system could not reach an equivalent or superior performance level. However, due to the budgetary constraints of this initial iteration those options were not financially viable.

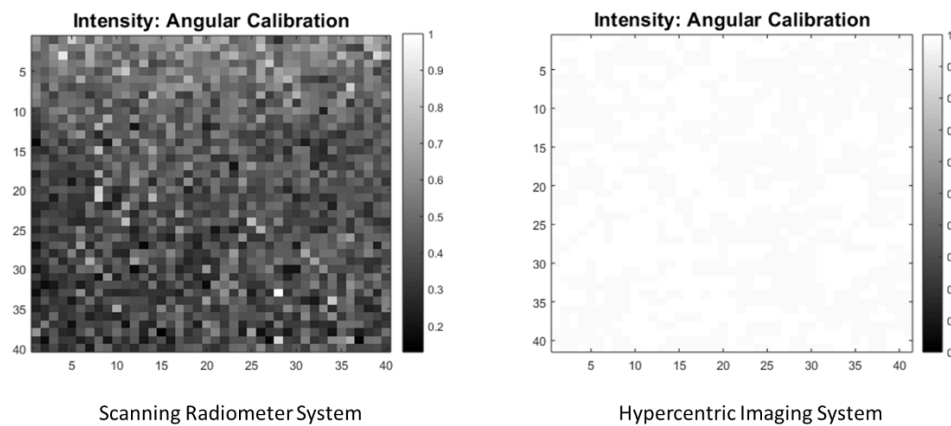


**Figure 18 – Angular Data Comparison:** Qualitative comparison of the noise levels offered for both the scanning radiometer system for angular uniformity (left) and the hypercentric imaging system for angular uniformity (right). Both images have been normalized for this relative comparison.

For the purposes of quantifying the noise of the “unwrapping” algorithm being used for converting the angular uniformity data, the CV at the edge of the aperture of the integrating sphere was also calculated. Figure 19 shows the entire process going from the initial image to isolation of the regions corresponding to the center of the output port and to the edge of the output port. These regions are highlighted to qualitatively show the



region the CV values were calculated for to determine the noise level of the system (central, blue region) and for the “unwrapping” algorithm (edge, red region).

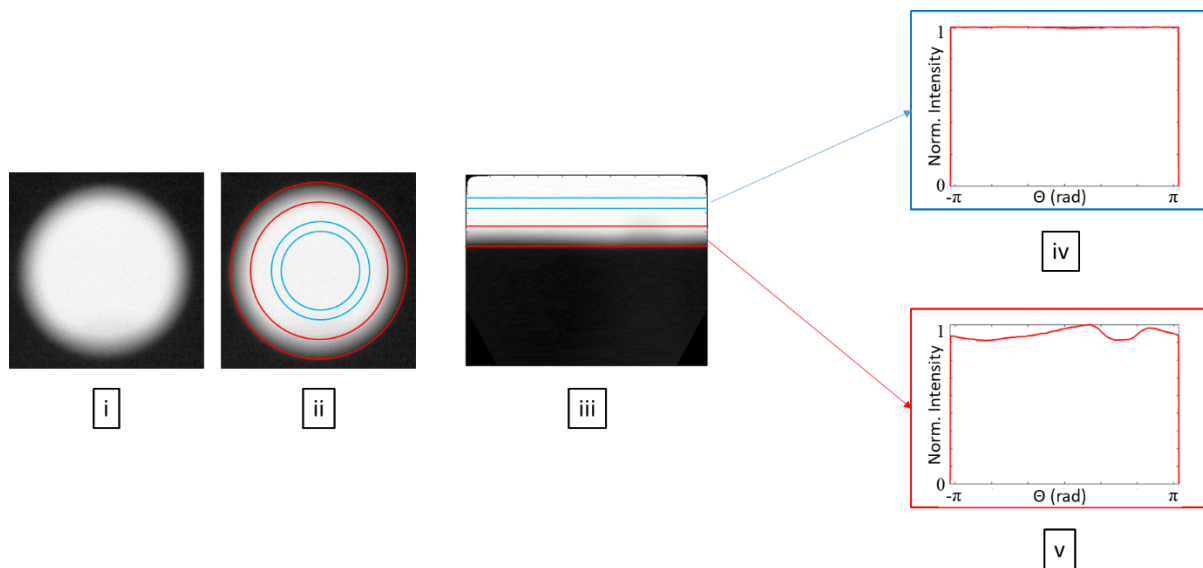


**Figure 19 – Analysis of Hypercentric Imaging System’s Integrating Sphere Data:**

from left to right this shows: i) the original image captured with the hypercentric imaging system of the output port of the integrating sphere ii) an overlay showing a blue outlined region toward the center and a red outlined region which covers the edge of the output port iii) The “unwrapped” image of the output port with these same red and blue regions outlined iv,v) plots of the uniformity of these regions vs theta with the center of the output port show at the top outlined in blue and the edge of the output port shown at the bottom outlined in red.

It’s important to note here that for the data presented later where the CV level for a larger bandwidth of R values is being calculated by summing the values at each theta position the impact of the noise related to the “unwrapping” algorithm is negligible. This leads to smoothing of the data which suppresses this noise. However, when looking to

evaluate 1) smaller R bands where smoothing will have less of an impact, 2) non-uniformities across R as well as theta, or 3) in cases where specific theta positions are being evaluated this must be considered.

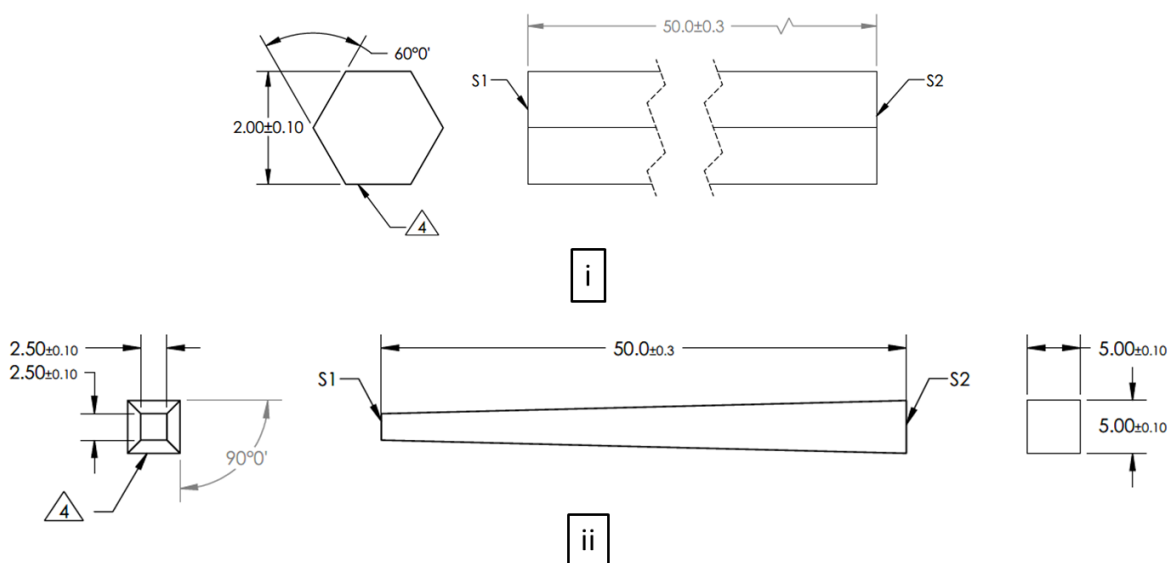
### ***Spatial Uniformity Noise Determination***

In order to quantify the noise level of the spatial uniformity measurements a similar process was followed. Given the clear advantage in the imaging based system during the angularity uniformity comparison, spatial uniformity data was only collected using the imaging based system. The CV calculated for this system was 0.0133, which is higher than the angular uniformity value calculated previously but still an order of magnitude below what is expected for the lightpipes.

# Experimentation

## Background

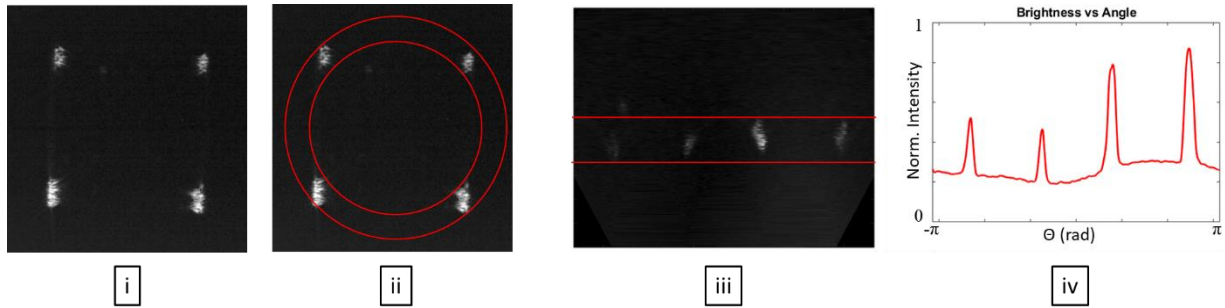
In order to evaluate the final spatial and angular uniformity test setups, and their ability to validate whether or not a given lightpipe is suitable for the applications discussed earlier, a simple case study was conducted. For this study two off the shelf lightpipes were selected and tested on both setups. The data collected for each was evaluated for suitability in the applications discussed earlier, as well as used to compare the two designs against one another. The two design forms chosen were that of a straight hexagonal lightpipe (#63-080, Edmund Optics Inc., Barrington, NJ, USA) and tapered square lightpipe (#63-103, Edmund Optics Inc., Barrington, NJ, USA). Figure 20 shows the exact dimensions of each.



**Figure 20 – Lightpipe Case Study Candidates:** (i) 2mm x 50mm long hexagonal lightpipe (ii) 2.5mm entrance face x 50mm long square tapered lightpipe.

## Results

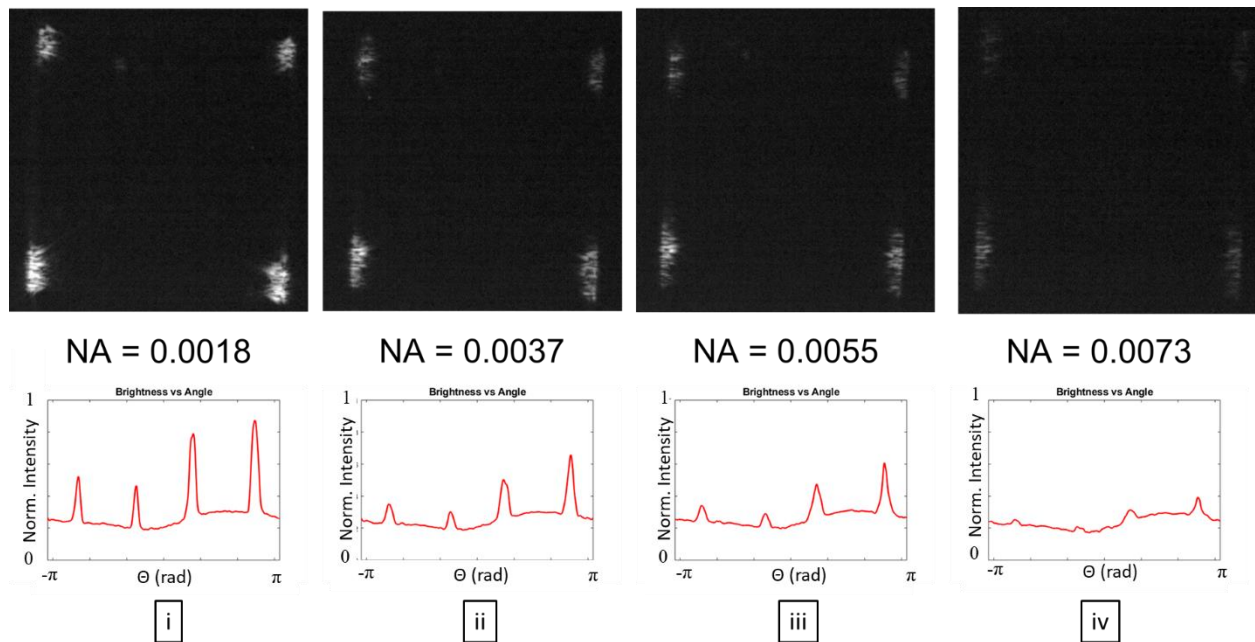
First the angular uniformity performance of both lightpipes was evaluated. From a simply qualitative standpoint we can see a difference in the intensity data captured from either design. The tapered lightpipe creates 4 distinct regions or peaks compared to only 3 for the hexagonal lightpipe. Also, it is clear that the shape of these regions are not necessarily oriented radially, which is shown in Figure 21(i) and 21(ii). When “unwrapping” the image we can see that these regions appear to be slightly angled as result as shown in Figure 21(iii). The last thing that is apparent is that any slight misalignment of the hypercentric lens to the lightpipe will also create an offset or ripple in the data. In the Figure 21(iii) there is a slight misalignment of the two peaks to the right compared to those on the left. This is the result of a slight decenter of the lightpipe output in the image.



**Figure 21 – “Unwrapping” Process of the Tapered Lightpipe Output:** (i) Image of the angular output of the square tapered lightpipe captured with the hypercentric imaging system. (ii) Shows the same image but with red outlines showing the R range over which uniformity will be analyzed. (iii) Shows the unwrapped image with the same region outlined. (iv) Plot of the normalized brightness vs theta for the highlight

region. Note the 4 peaks which correspond to the 4 bright spots shown in the previous images.

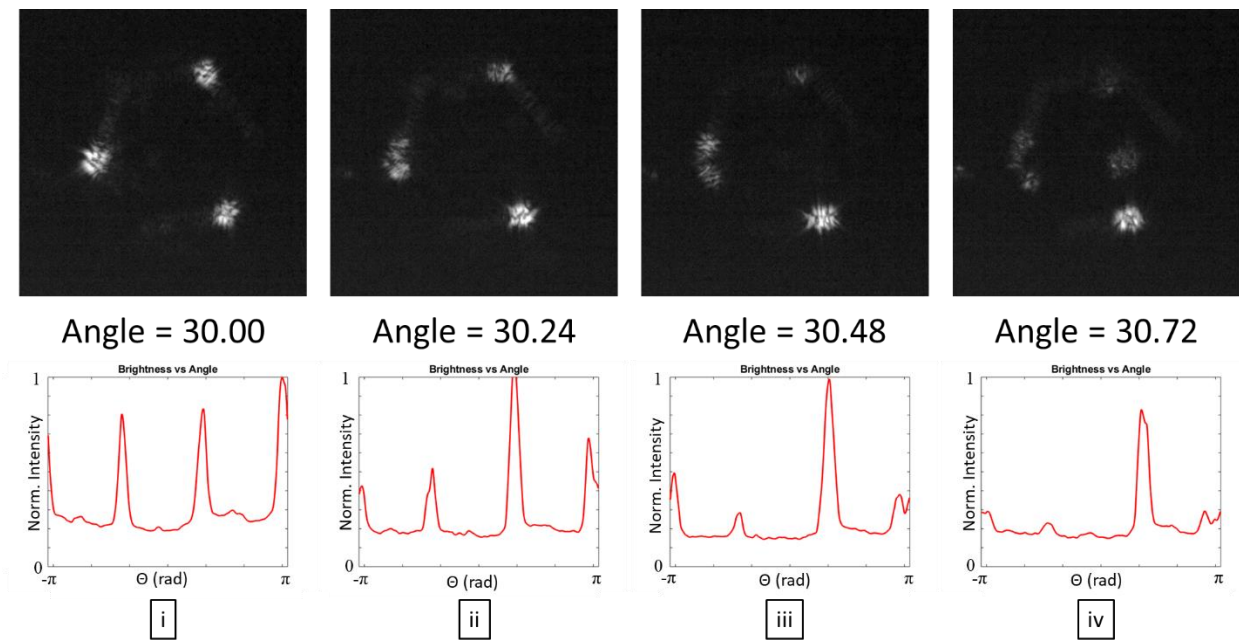
As mentioned earlier, ideally misalignments like this will be adjusted out during the initial setup, however, it can also be compensated for in the data analysis. For the purposes of this case study the values over a given R bandwidth were summed for each  $\theta$  position. This also helps overcome any ripple in the output profile data after the radial unwrapping. Figure 21(iv) shows the resulting 1D profile, which clearly shows the 4 distinct peaks seen in the original image.



**Figure 22 – Change in Uniformity vs Numerical Aperture:** This figure shows how as the numerical aperture of the input light increases the uniformity of the output of the lightpipe improved. Data shown is for the square tapered lightpipe. (ii) Image and normalized brightness data for NA = 0.0018. (ii) Image and normalized brightness

data for NA = 0.0037. (iii) Image and normalized brightness data for NA = 0.0055. (iv) Image and normalized brightness data for NA = 0.0073.

This process was used to capture and analyze data for both lightpipe designs, and evaluate the change in angular uniformity as the NA of the input light was increased. As shown in Figure 22, increasing the NA smooths the intensity profile of the square tapered lightpipe, yielding improved uniformity as expected. By expanding the original input beam diameter and NA the radiant intensity is redistributed over a greater range of angles leading to the improved uniformity being observed. There is a tradeoff between improved uniformity over angle at the output at the sacrifice of the peak intensity.



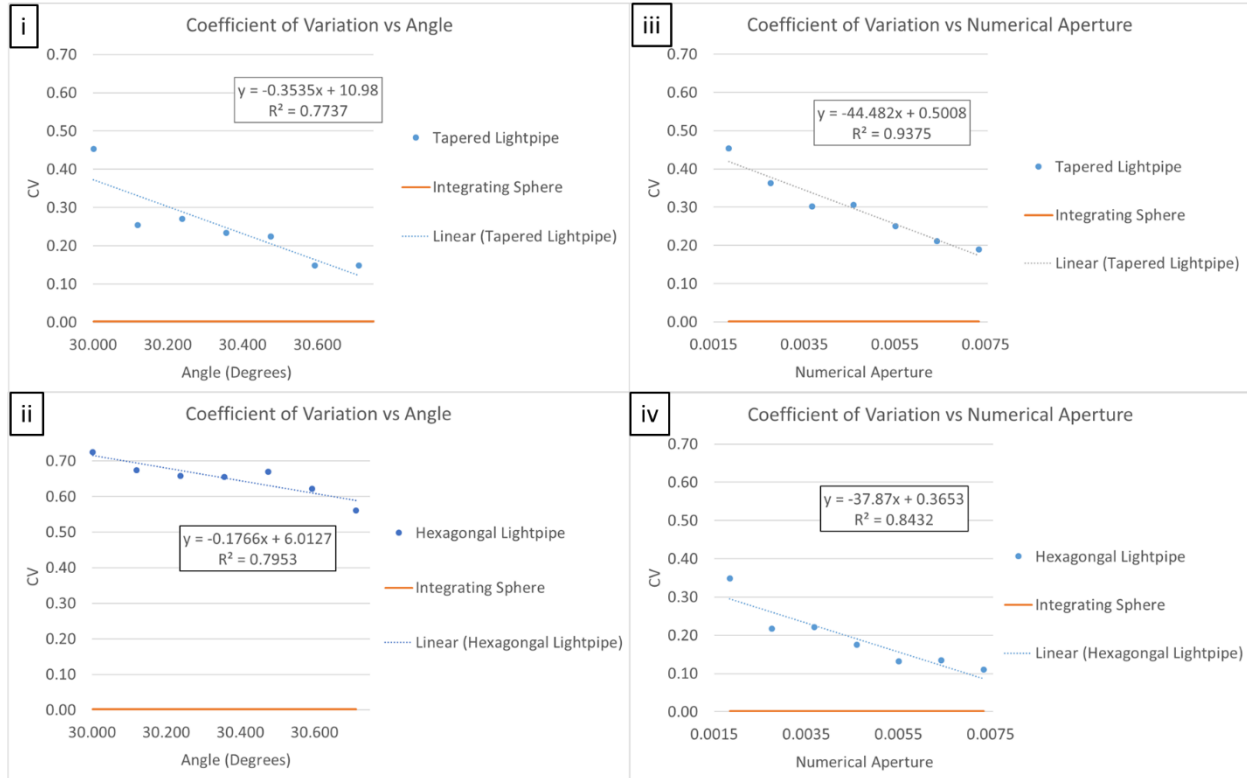
**Figure 23 – Change in Uniformity vs Input Angle:** This figure shows how as the input angle of the light entering the lightpipe increases the uniformity of the output of the lightpipe improved. Data shown is for the straight hexagonal lightpipe. (i)

Image and normalized brightness data for Angle = 30.00 (ii) Image and normalized brightness data for Angle = 30.24 (iii) Image and normalized brightness data for Angle = 30.48 (iv) Image and normalized brightness data for Angle = 30.72

Similarly as the angle of the gut ray of the input cone is increased we should see the intensity uniformity of both designs should also increase. Even though the change in angle created here is small in theory this should increase the number of reflections per unit length which will improve the uniformity. Figure 23 shows the effects of increasing the input angle when using the straight hexagonal lightpipe. While all of the peaks are not smoothed equally as the input angle increases, the overall uniformity does improve.

Reviewing the total angular uniformity CV data collected for both lightpipes, the effects shown in Figures 22 and 23 regarding increasing the NA of the input beam and increasing the input angle of the input beam are confirmed. Figure 24 is a summary of all the angular CV data collected. Figures 24(i) and 24(ii) show the correlation between input angle and the resulting angular uniformity CV value for the square tapered lightpipe and the straight hexagonal lightpipe respectively. Similarly Figures 24(iii) and 24(iv) show the correlation between input beam NA and the resulting angular uniformity CV value for the square tapered lightpipe and the straight hexagonal lightpipe respectively. In all 4 cases there is strong correlation as we would expect, however, what is interesting is that when comparing the two designs the rate of change is higher for the tapered lightpipe compared to the straight lightpipe. Intuitively this makes sense as the tapered design inherently creates a change in angle from input to output, and now by increasing the input angle or NA on top of that a compounding effect is created. Also, the strength of the correlation between

NA and the angular uniformity CV value is higher than that of the input angle and angular uniformity CV value.



**Figure 24 – Summary of CV Data for Angular Uniformity Measurements:** (i) Plot of the change in angular uniformity CV value vs illumination input angle over a constant NA for the square tapered lightpipe. (ii) Plot of the change in angular uniformity CV value vs illumination input angle over a constant NA for the straight hexagonal lightpipe. (iii) Plot of the change in angular uniformity CV value vs NA over a constant input angle for the square tapered lightpipe. (iv) Plot of the change in angular uniformity CV value vs NA over a constant input angle for the straight hexagonal lightpipe.



The effect of changes to the input angle and NA on the spatial uniformity are quite different. Figures 25(i) and 25(ii) show the correlation between input angle and the resulting spatial uniformity CV value for the square tapered lightpipe and the straight hexagonal lightpipe respectively. Similarly Figures 25(iii) and 25(iv) show the correlation between input beam NA and the resulting spatial uniformity CV value for the square tapered lightpipe and the straight hexagonal lightpipe respectively.

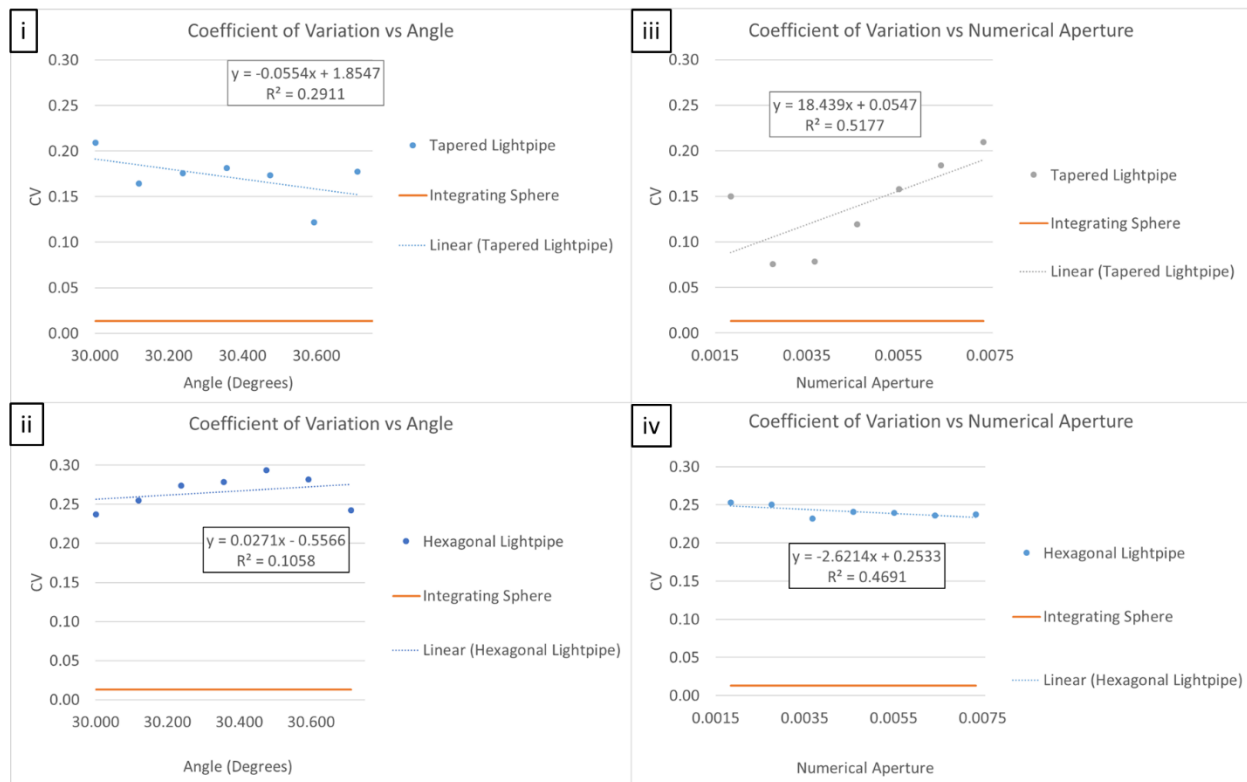


**Figure 25 – Summary of CV Data for Spatial Uniformity Measurements:** (i) Plot of the change in spatial uniformity CV value vs illumination input angle over a constant NA for the square tapered lightpipe. (ii) Plot of the change in spatial uniformity CV value vs illumination input angle over a constant NA for the straight hexagonal lightpipe. (iii) Plot of the change in spatial uniformity CV value vs NA over

a constant input angle for the square tapered lightpipe. (iv) Plot of the change in spatial uniformity CV value vs NA over a constant input angle for the straight hexagonal lightpipe.

Overall the spatial uniformity CV values for each design are quite low compared to the angular uniformity CV data reviewed earlier, but overall the spatial data shows a much lower correlation. In fact based on the level of correlation observed in the spatial uniformity CV data it is fair to question if the changes the input angle and NA offered by the current testbed are significant enough to have an effect on the spatial uniformity. The angular uniformity CV data was dominated by the overall profile and the distinct peaks, with light only present in a select bandwidth with respect to R, and at certain regions of theta. The coherence of the source can be observed but it is on a much smaller in scale than the overall intensity profile. This is not case however in the irradiance profile.

In the spatial data set the entire field of view is filled with light and the variations observed look to be mainly driven by the coherence in our source. This means that the changes to the spatial uniformity CV due to the changes in angle and NA are far less impactful in comparison to the coherence effects. Qualitatively changes to the coherence pattern, the finer texture of the irradiance profile can be observed, but the overall uniformity is generally the same. This makes it clear that in order to capture the observed changes to the finer details in the irradiance profile an alternative metric is necessary.

In order to capture these changes to the coherence pattern the PSD of the irradiance profile was examined. The PSD of the 2D irradiance profile helps to highlight the underlying periodic spatial frequencies of the coherence observed. As a reference the PSD

of the integrating sphere data reviewed earlier was calculated. This generally follows the linear PSD profile one would expect for a uniform 2D irradiance profile.

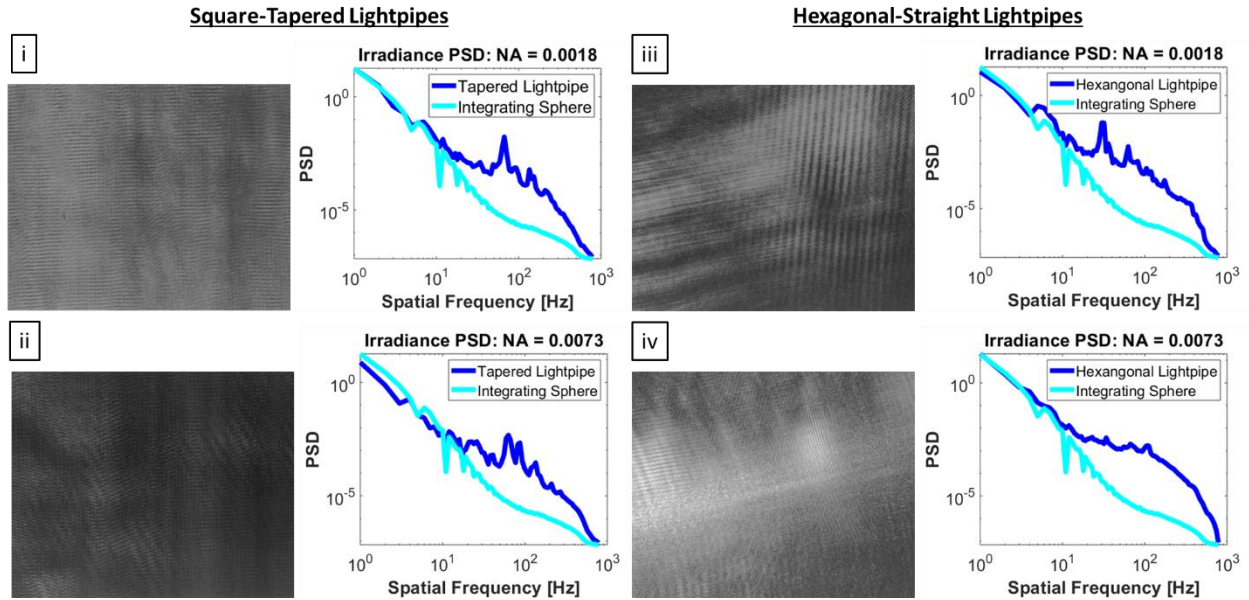


**Figure 26 – Summary of PSD Data for Spatial Uniformity Measurements:**

Comparison of 4 different configurations of lightpipe design and NA to highlight differences in the coherence pattern of each based on the PSD. (i) Image of the irradiance output of the square tapered lightpipe with a 0.0018 NA input, along with the corresponding PSD of this 2D irradiance profile. (ii) Image of the irradiance output of the square tapered lightpipe with a 0.0073 NA input, along with the corresponding PSD of this 2D irradiance profile. (iii) Image of the irradiance output of the straight hexagonal lightpipe with a 0.0018 NA input, along with the corresponding PSD of this 2D irradiance profile. (iv) Image of the irradiance output of the straight hexagonal lightpipe with a 0.0073 NA input, along with the corresponding PSD of this 2D irradiance profile.

Figure 26 summarizes the results of this PSD analysis. Figures 26(i) and 26(ii) compare the measured PSD of the square tapered lightpipe with an input beam NA of 0.0018 and 0.0073 respectively, with the raw image for the 2D irradiance profiles for each also shown. Figures 26(iii) and 26(iv) compare the measured PSD of the straight hexagonal lightpipe with an input beam NA of 0.0018 and 0.0073 respectively, with the raw image for the 2D irradiance profiles for each also shown. We can see in the 0.0018 NA case for both lightpipes (Figure 26 i & ii) there is a distinct peak spatial frequency for the coherence pattern, though the exact peak frequency for each design is slight different. This is likely due to the angular change induced by the tapered design. Then upon increasing the NA (Figure 26 iii & iv) these peaks are suppressed and the overall PSD profile of each is broadened. This implies that by increasing the NA of the input results in further breakdown of the coherence of the irradiance profile as expected.

## Conclusions & Future Considerations

Based on the results of this case study it is clear that the tapered design offers superior performance in terms of uniformity. We can clearly see that the change in angle created by the lightpipe design itself offers a clear advantage. When this is coupled with a higher NA input source and large chief ray input angle these angles stack up to increase the degree of uniformity further. This does come at the expense of etendue, but if uniformity spatially and angularly is more important in an application than efficiency and light throughput this design could be an option.

Looking back at the uniformity requirements of the two applications we discussed, and their illumination requirements however we see that even the better of the two lightpipe designs may not be good enough. Recall that the uniformity required for flow cytometry was  $< 14\%$  while the measured spatial and angular uniformity CV values at best ranged from 0.15 to 0.25. Being that all of our data sets are normalized we can correlate this CV range of 0.15 to 0.25 to be equal to a 15% to 25% variation which is not sufficient. The same is true for possibly using this lightpipe design in a DLP projector. There the uniformity target was actually 10%.

However, taking a step back we stated in the introduction that the goal of this study was not to develop a solution for how to combine these sources, but rather to develop an inspection system for quantifying how effective possible solutions are. Serving as an initial trade study to review the two main system options measuring irradiance and radiant intensity uniformity this study was a success. The angular uniformity setup is able to

measure uniformity across a range of  $\pm 33$  degrees, comfortably exceeding the  $\pm 17$  degrees of the DMD in the DLP projectors discussed, with better than 4 arcsec angular resolution. The spatial uniformity setup offers a resolution down to 0.265 $\mu\text{m}$  exceeding all of the requirements discussed for flow cytometry and digital cinema projectors other than the 0.2 $\mu\text{m}$  resolution of the SCD in the flow cytometer reviewed in detail.

Furthermore having focused on the imaging based solutions for this initial proof-of-concept system, which only utilized off the shelf components, the initial case study presented shows this concept has merit as a lightpipe testbed for investigating uniformity. Both the angular and spatial test setups offer the ability to differentiate the performance of the two design forms investigated here, where the calculated uncertainties in each setup were at least an order of magnitude less than the measured values for each lightpipe. The measured correlation in the angular uniformity data regarding changes to the NA and input angle was also very high as expected, with the increase the degree of angular uniformity quantified in terms of CV.

That said there is certainly room for improvement in the next iteration of this testbed design. While there is a relatively high correlation in the angular uniformity CV data it is rather noisy. Also, the spatial CV data was too noisy to draw any conclusions. This is partly due to the fact that the spatial uniformity is less sensitive to limited range of angles available in the current testbed, but is also likely limited by the tolerances of the mechanics used in the coherent illumination system. In particular, the tolerances of the linear translation stage and its mounting are an area for future improvement. The current plate and adapters the stage is bolted to offer an angular tolerance of  $\pm 0.25$  degrees, while the stage itself offers an angular deviation of 30 arcsecs.

The runout in the plate and adapters in theory can be trammed out, but in practice with these looser tolerances this is quite difficult to accomplish. By designing a custom plate which has datums and tolerances specific to the setup, defined based on this alignment process, the resulting performance of the system can be improved significantly. Also, moving away from an aluminum stage to a stainless steel version with an angular deviation of 20 arcsecs rather than the current 30 arcsec tolerance will also help improve the system.

The issue here is that the design is optimal assuming we have a collimated input beam incident to the OAP which is perfectly aligned with the axis of the mirror. For even a slight angular misalignment of the input beam with respect to the OAP the focus spot of the mirror within the lightpipe changes position which will affect the output profile. In order to generate the most mixing and therefore uniformity the system is aligned so that the focus spot is directed at one of the intersections of the side walls of the lightpipe. This creates a splitting of the input beam which further redistributes the light. Small shifts in the input angle that result in a shift in this focus position will interfere with this splitting effect.

Figure 27 contains non-sequential modeling data to illustrate this. In Figure 27(i) the model is setup such that there is a perfectly collimated beam traveling on-axis with respect to the OAP to the right in the image. The focus point in this situation is perfectly aligned with the intersection of two of the sidewalls in the straight hexagonal lightpipe design. Taking a close look at the rays going through the lightpipe the splitting can be observed, where it occurs near the input of the lightpipe and by the midpoint we can see two separate ray bundles now traveling down the lightpipe. In figure 27(ii) the beam incident on the OAP is misaligned by 0.25 degrees. Taking a closer look at the rays traveling

through the lightpipe they appear to be traveling together now throughout the lightpipe, not in two separate bundles as the splitting has been interrupted to some degree.

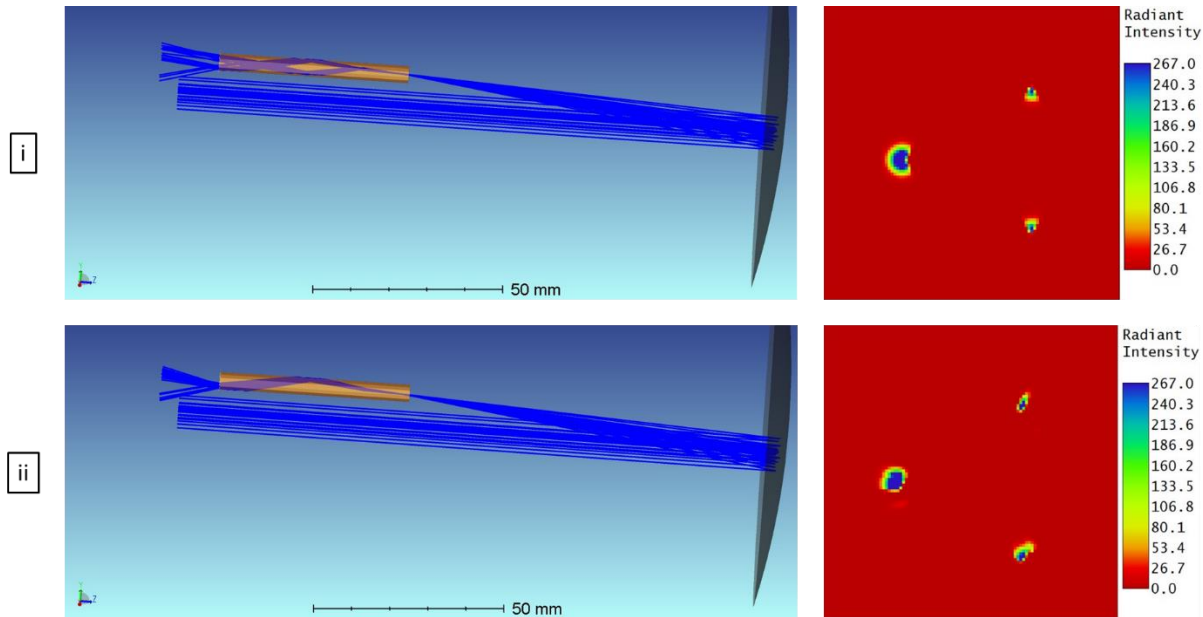


**Figure 27 – Non-Sequential Modeling of Alignment Errors:** (i) Shows the ray trace and corresponding radiant intensity plot when the focus spot from the parabolic mirror is aligned perfectly with the intersection of two of the sidewalls of the lightpipe. In this configuration the input beam is split evenly as observed in the ray diagram, leading to an even split in the radiant intensity between the two regions corresponding to the secondary reflections. (ii) Shows the ray trace and corresponding radiant intensity plot when the focus spot from the parabolic mirror is misaligned by 0.25 degrees. In this configuration the input beam is not split evenly about the intersection of the two sidewalls, leading to an uneven split in the radiant intensity between the two regions corresponding to the secondary reflections.



Taking a closer look at the radiant intensity output profiles for both we can see a clear difference. In both cases there is a region which corresponds to the first reflection in the lightpipe, which is the region containing the highest radiant intensity. When the focus is aligned perfectly with the sidewall intersection there is an even distribution of the light between the other two regions corresponding to the second reflection for each split bundle. In the case where the input beam is misaligned with the OAP and the focus spot is translated creating an uneven split the regions corresponding to the secondary reflections in the radiant intensity output. This means that any change in the pointing stability of the system over the range of motion of the translation stage is going to vary the output distributions. This will create a source of error in the measurement, making it harder to quantify any changes resulting from the intended change in input angle.

Furthermore, the OAP itself could be replaced with one that has tighter tolerances. The current mirror is specified to have surface irregularity of  $\frac{1}{4}$  wave RMS which equates roughly to 1-1.5 wave PV or  $\sim 1\mu\text{m}$ . As the input beam translates across the mirror to create the change in input angle it is going to experience a local change in pointing of up to  $1\mu\text{m}$  as a result of this surface irregularity. The current mirror also offers a surface roughness of  $< 174\text{\AA}$  RMS where tighter tolerance versions offer as low as  $< 50\text{\AA}$  RMS. This roughness is going to create additional scatter where again local changes to the roughness are going to affect the efficiency of the system. Also, the mirror will have some periodic structure which may not be necessarily captured by the roughness specification. This periodic structure is a result of the tooling path from the diamond turning machine used to make the mirror. This could also be a source of variation across the mirror, where the cutting angle of the tool may change over the surface of the part. This type of change in cutting angle of the tool over

the parts will result in a change of the spatial frequency of the tool marks. If a custom mirror were to be specified for the testbed then requirements could be included to constrain these sources of error induced by the mirror.

Last, with a custom hypercentric lens the resolution and FOV of the angular test setup could be increased. This version of the hypercentric test setup is limited to a maximum viewing angle of 33 degrees and a maximum camera sensor of 2/3". Bearing in mind that in order to have adequate sensitivity to low light levels and reduced sensor noise the pixel size should be 4-5um at least, this effectively limits the resolution achieved with the current lens. A custom design which offers a larger maximum sensor size, would allow for increased resolution while maintaining the current pixel size. Also, increasing the maximum viewing angle of the lens would give the test setup more flexibility. This would allow for testing at a higher input angle for the illumination coming into the lightpipes. This is ideal as it should increase the number of reflection per unit length in the lightpipe, which will in turn provide better uniformity.

# References

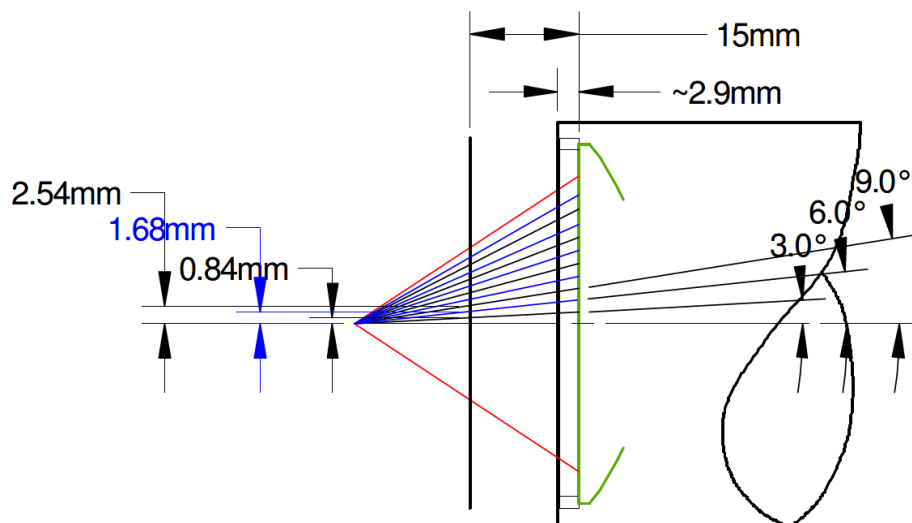
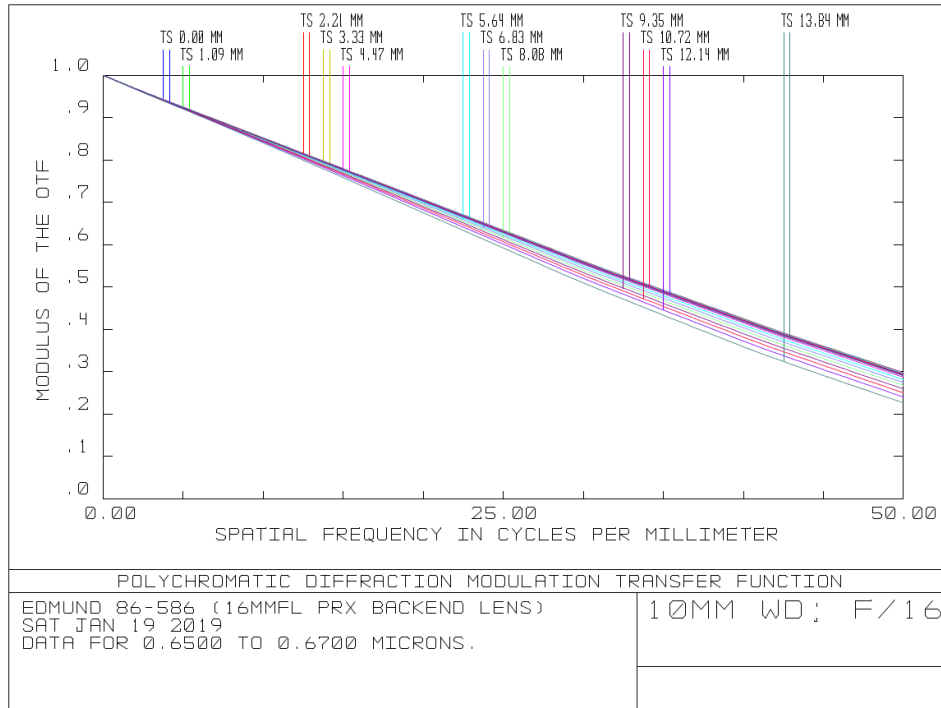
- [1] R. Koshel, *Illumination Engineering: Design with Nonimaging Optics*, Piscataway, NJ: John Wiley & Sons, 2013.
- [2] Christie Digital System USA, Inc., "Cinema laser projection: Illumination options for your cinema," 2017. [Online]. Available: <https://www.christiedigital.com/TechPapers/Cinema-laser-projection-Illumination-options-for-your-cinema.pdf>. [Accessed 27 April 2019].
- [3] Eiki International, Inc., "Some Pros and Cons of LED vs. Laser Projectors," [Online]. Available: <https://www.eiki.com/eiki-faqs/some-pros-and-cons-of-led-vs-laser-projectors/>. [Accessed 27 April 2019].
- [4] NEC Display Solutions, "NEC Display Solutions of America - Laser Projector Solutions," [Online]. Available: <https://www.necdisplay.com/laser-projectors/laser.html>. [Accessed 27 April 2019].
- [5] G. Finch, "What to Look for in a DLP Projector," ViewSonic, 20 November 2018. [Online]. Available: <https://www.viewsonic.com/library/entertainment/what-look-for-dlp-projector>. [Accessed 8 April 2019].
- [6] Texas Instruments, "DLP Products: Standard Shipsets," January 2017. [Online]. Available: <http://www.ti.com/dlp-chip/display-and-projection/standard-chipsets/products.html>. [Accessed 3 March 2018].
- [7] Texas Instruments Incorporated, "Single-Panel DLP Projection System Optics," Texas Instruments, Dallas, 2005.
- [8] Epson, "Pro L1100U Laser WUXGA 3LCD Projector w/ 4K Enhancement & Standard Lens," [Online]. Available: <https://epson.com/For-Work/Projectors/Large-Venue/Pro-L1100U-Laser-WUXGA-3LCD-Projector-w-4K-Enhancement-%26-Standard-Lens/p/V11H735020>. [Accessed 25 March 2018].
- [9] Navitar, "Custom Conversion Lens Solutions for Small Format 4K," [Online]. Available: <https://navitar.com/products/projection/4k-screenstar-lens-kits/custom-conversion-lens-solutions-small-format-4k/>. [Accessed 25 March 2018].
- [10] R. R. Jahan-Tigh, C. Ryan, G. Obermoser and K. Schwarzenberger, "Flow Cytometry," *Journal of Investigative Dermatology*, vol. 132, 2012.
- [11] P. Ladurner, "Regeneration and Neoblasts," European Research Institute for the Biology of Ageing, [Online]. Available: <http://www.macgenome.org/neoblasts.html>. [Accessed 20 April 2019].

- [12] Bio-Rad Laboratories, Inc., "Flow Cytometry Basics Guide," [Online]. Available: <https://www.bio-rad-antibodies.com/static/2016/fc-guide/flow-cytometry-basics-guide.pdf>. [Accessed 25 April 2019].
- [13] S. Piatek and E. Hergert, "Photodetectors In Flow Cytometry," *Photonics Spectra*, pp. 44-47, December 2018.
- [14] A. L. Givan, *Flow Cytometry: First Principles*, Second Edition, New York: John Wiley & Sons, Inc., 2001.
- [15] Stratedigm, Inc., "S1000EXi Benchtop Flow Cytometer," [Online]. Available: <https://stratedigm.com/s1000exi-flow-cytometer/?>. [Accessed 3 March 2018].
- [16] R. A. Hoffman and J. C. Wood, "Characterization of Flow Cytometer Instrument Sensitivity," in *Current Protocols in Cytometry*, John Wiley & Sons, Inc., 2007, pp. 1.20.1-1.20.18.
- [17] E. Schonbrun, P. E. Steinvurzel and K. B. Crozier, "A microfluidic fluorescence measurement system using an astigmatic diffractive microlens array," *Optics Express*, vol. 19, no. 2, pp. 1385-1394, 2010.
- [18] B. R. Watts, T. Kowpak, Z. Zhang, C.-Q. Xu and S. Zhu, "Formation and characterization of an ideal excitation beam geometry in an optofluidic device," *Biomedical Optics Express*, vol. 1, no. 3, pp. 848-860, 2010.
- [19] Newport Corporation, "Dichroic Laser Beam Combiners," 17 March 2018. [Online]. Available: <https://www.newport.com/f/dichroic-laser-beam-combiners>.
- [20] W. J. Cassarly and T. L. R. Davenport, "Non-rotationally symmetric mixing rods," in *Proceedings of SPIE*, San Diego, 2006.
- [21] V. Arecchi, *Field Guide to Illumination Optics*, Bellingham, WA: SPIE Press, 2007.
- [22] D. Williamson, "Cone Channel Condenser Optics," *Journal of the Optical Society of America*, pp. 712-715, 1952.
- [23] R. Leutz and H. Ries, "Squaring the circle: use of microstructures for converting and homogenizing beam patterns," in *Proceedings of SPIE*, San Diego, 2003.
- [24] E. Hecht, *Optics*, 4th ed., New York: Addison Wesley, 2002.
- [25] RP Photonics Consulting GmbH, "Coherence," [Online]. Available: <https://www.rp-photonics.com/coherence.html>. [Accessed 20 April 2019].
- [26] E. Salik, "Optical Phase Measurement Emphasized," in *Education and Training in Optics and Photonics*, St. Asaph, North Wales United Kingdom, 2009.

- [27] M. Wagner, H. D. Geller and D. Wolff, "High-performance laser beam shaping and homogenization system for semiconductor processing," *Measurement Science and Technology*, pp. 1193-1201, 1990.
- [28] J. M. Palmer and B. G. Grant, *The Art of Radiometry*, Bellingham: SPIE Press, 2010.
- [29] Light Works, LLC, "Why Hypercentric?," 2019. [Online]. Available: <https://lw4u.com/index.php/hypercentric-lenses/how-they-work/>. [Accessed 15 April 2019].
- [30] J. M. Geary, "Channel integrator for laser beam uniformity on target," *Optical Engineering*, pp. 972-977, 1988.
- [31] D. G. Pelli and P. Bex, "Measuring contrast sensitivity," *Vision Research*, no. 90, pp. 10-14, 2013.

# Appendix A

## Hypercentric Lens Data



## Appendix B

### ***Radiometer RSS Line-Of-Sight (LOS) Error***

For the purposes of the relative spatial and angular uniformity measurements included in this study it was deemed that the line-of-sight error the radiometer did not need to be considered. However, for testing which requires measurement to be made with respect to a global coordinate system this must be incorporated into the uncertainty of the system.

<b>Radiometer LOS Error</b>			
<b>Lens &amp; Holder:</b>			$\epsilon$ (mm)
Index of Refraction	1.458		
Focal Length (mm)	100		
Lens Thickness (mm)	2.44		
Lens Beam Deviation (deg)	0.0167		0.0291
Seat Tilt (deg)	0.25		0.0033
Decenter within Seat (mm)	0.05		0.05
		Total	0.082
<b>Aperture:</b>			
Diameter Tolerance (mm)	0.4		0.4
Alignment Accuracy (mm)	0.05		0.05
		Total	0.050
<b>RSS Image Motion (mm)</b>			0.096
<b>RSS Point Accuracy (urad)</b>			16.827